Supporting Information

Laser-Engineered Microcavity Surfaces with a Nanoscale Superhydrophobic Coating for Extreme Boiling Performance

Matic Može[a,*], Matej Senegačnik[a], Peter Gregorčič[a], Matej Hočevar[b], Matevž Zupančič[a,*], Iztok Golobič[a]

[a] *Faculty of Mechanical Engineering, University of Ljubljana, Aškerčeva 6, 1000 Ljubljana, Slovenia*
[b] *Institute of Metals and Technology, Lepi pot 11, 1000 Ljubljana, Slovenia*

Corresponding authors:
* E-mail: matic.moze@fs.uni-lj.si (M. Može)
* E-mail: matevz.zupancic@fs.uni-lj.si (M. Zupančič)

Table of Contents

S8.   Comparison of boiling performance of all surfaces

Figure S22. Comparison of boiling curves for all tested surfaces.

S9.   Surface stability

Figure S23. Evaluation of surface stability through repeated boiling tests on hydrophobized surfaces HPO VS 1, HPO VS 3 and HPO ES 1.

S10.   Experimental setup

Figure S24. Schematic depiction of the experimental setup for boiling performance measurement.

Figure S25. Cross section of the heater assembly part of the experimental setup.

Figure S26. Schematic depiction of the data acquisition part of the experimental setup.

S11.   Validation of the dynamic measurement approach

Figure S27. Validation of dynamic boiling heat transfer performance measurement.

Figure S28. Normalized heat flux versus axial distance along the copper heating stem and the aluminum sample for different heating rates. The inset stem drawing is not to scale.

Table S3. Normalized measured "average" heat flux between the thermocouples in the copper stem and normalized actual heat flux at the boiling surface.

S12.   Effect of working fluid degassing

Figure S29. Evaluation of the effect of proper working fluid degassing on surface HPO FT.

S13.   Data reduction and measurement uncertainty calculation

Table S4. List of uncertainties of contributing parameters.

S14.   References

S1.   SEM images of fabricated surfaces

Figures S1-S10 show SEM images of fabricated surfaces after they were exposed to boiling.
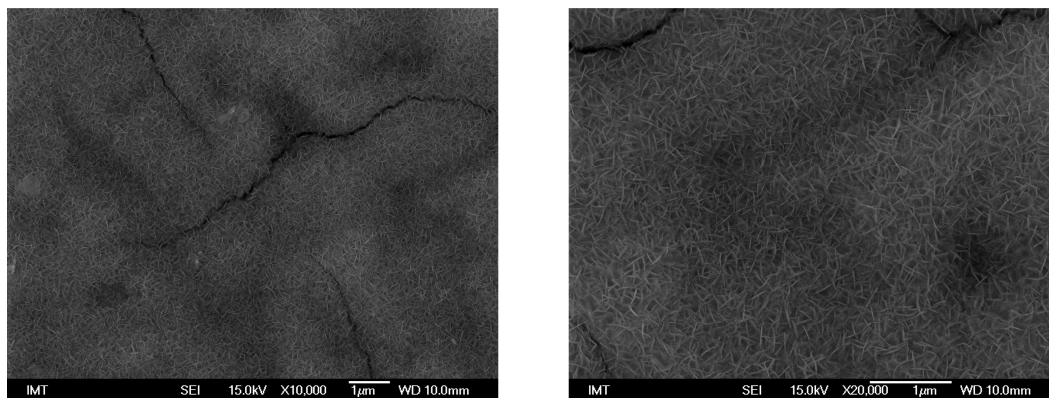
Figure S1. SEM images of the untreated reference surface (REF).
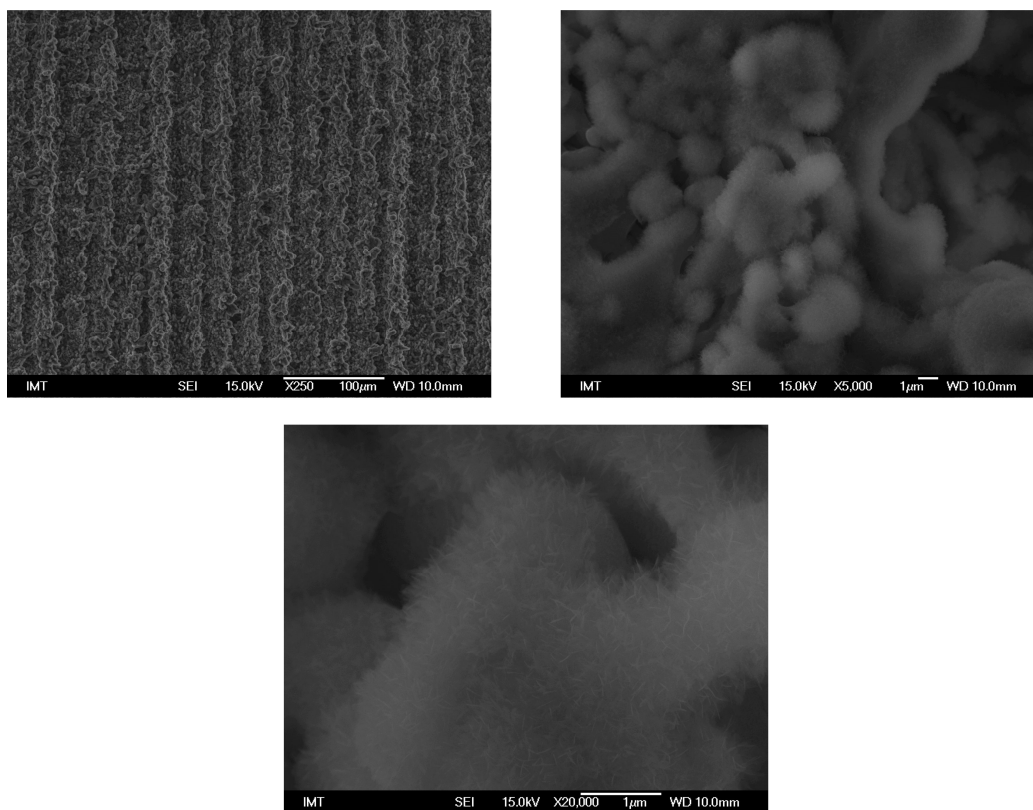
Figure S2. SEM images of the hydrophobized fully textured surface (HPO FT).
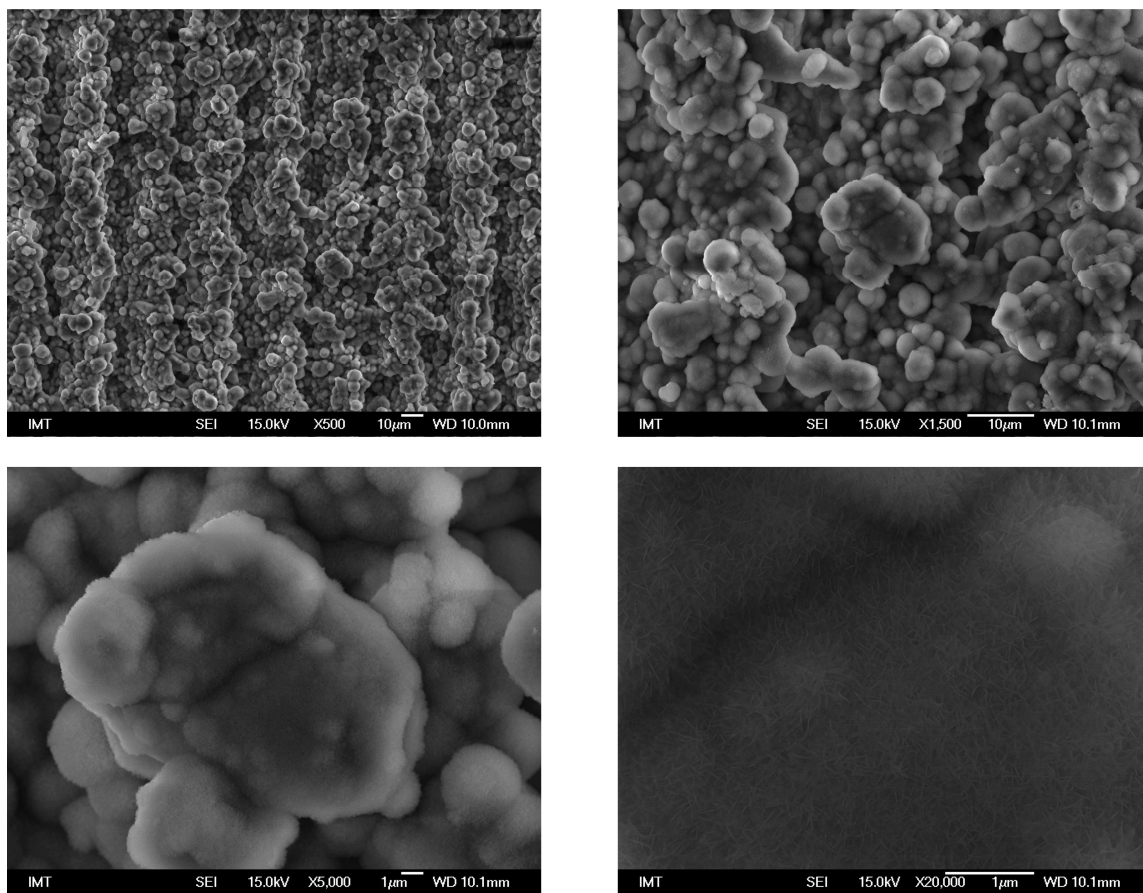
Figure S3. SEM images of the fully textured surface (HPI FT).
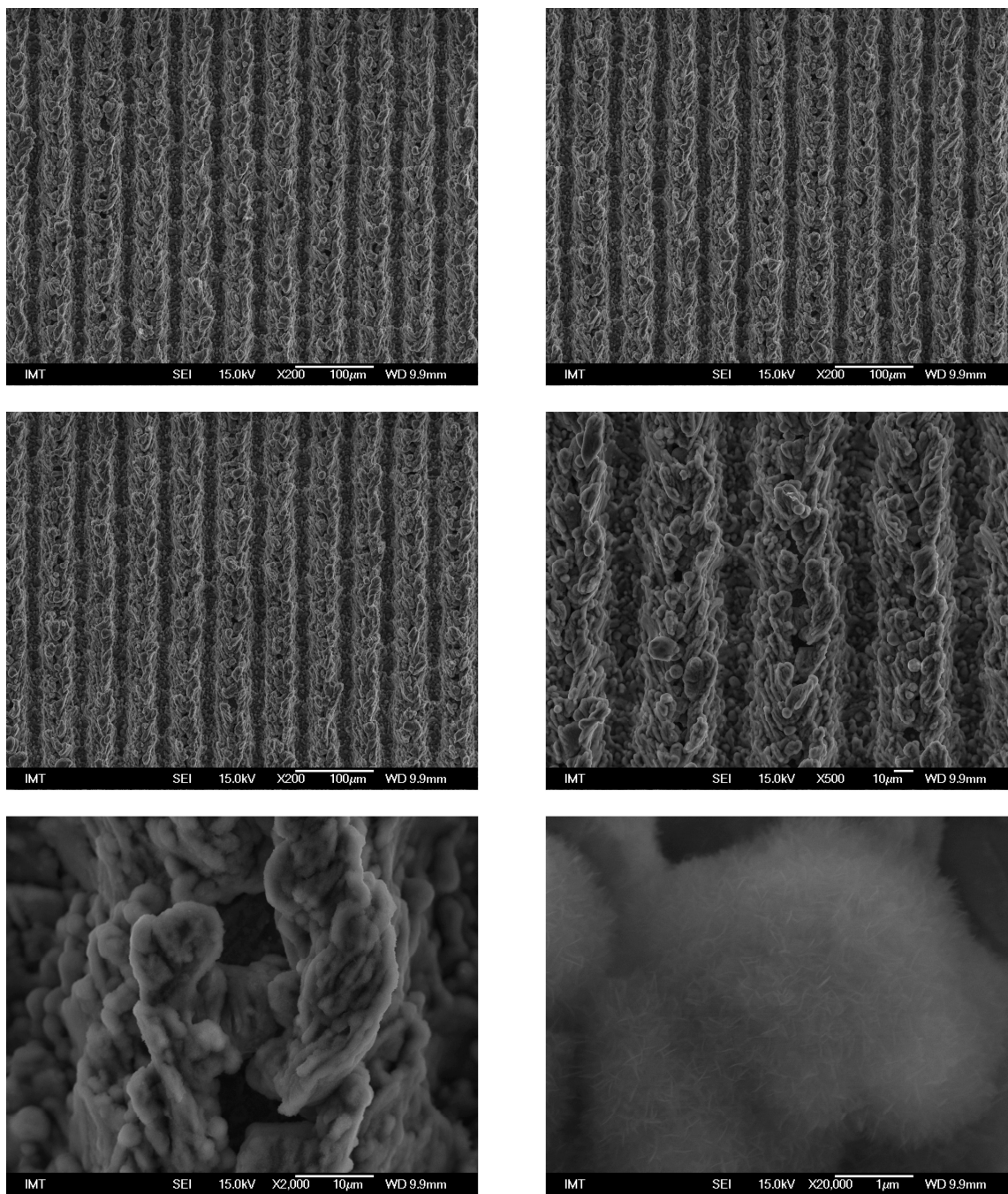
Figure S4. SEM images of the hydrophobized variable separation microcavity surface (HPO VS 1).
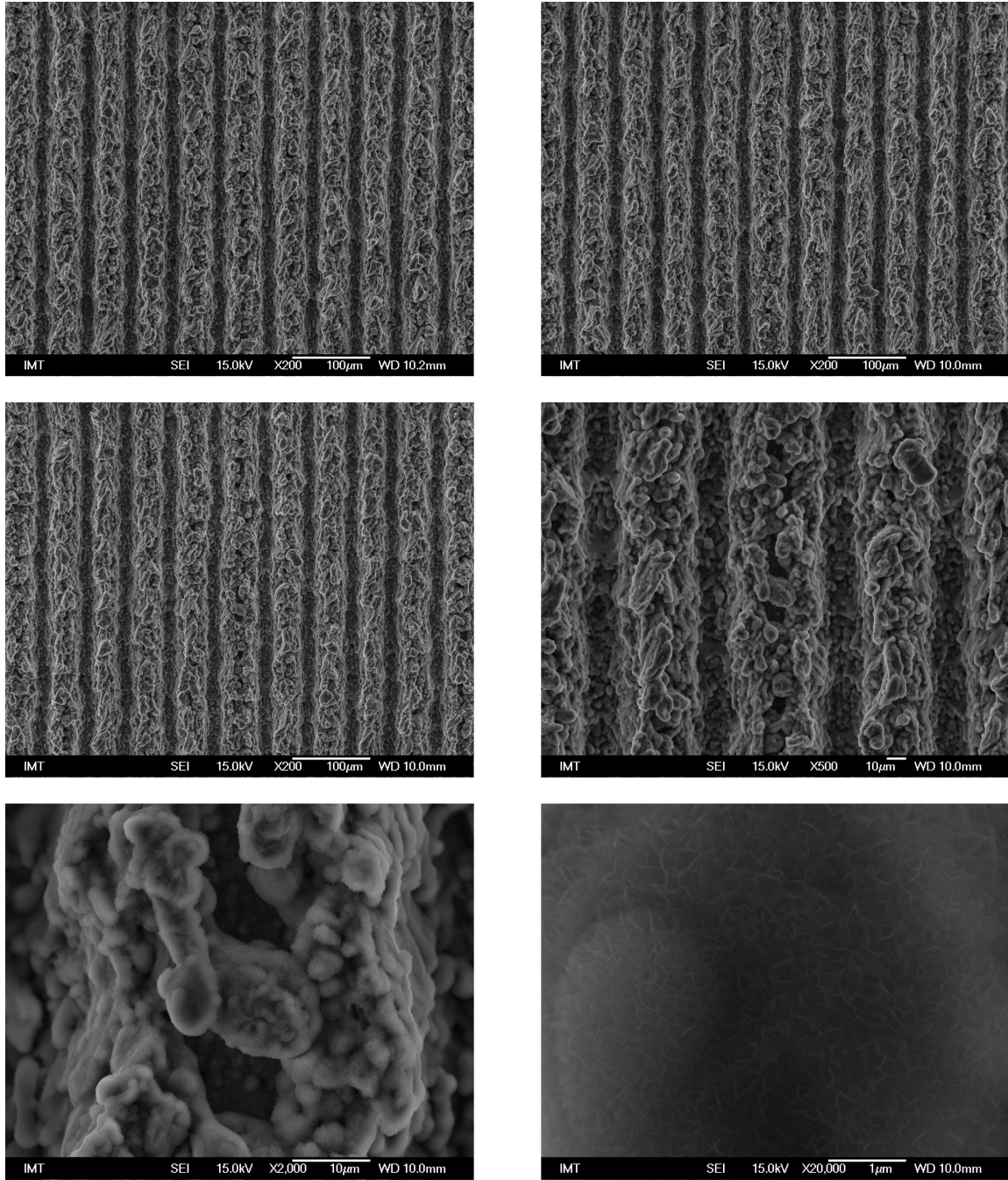
Figure S5. SEM images of the hydrophobized variable separation microcavity surface (HPO VS 2).
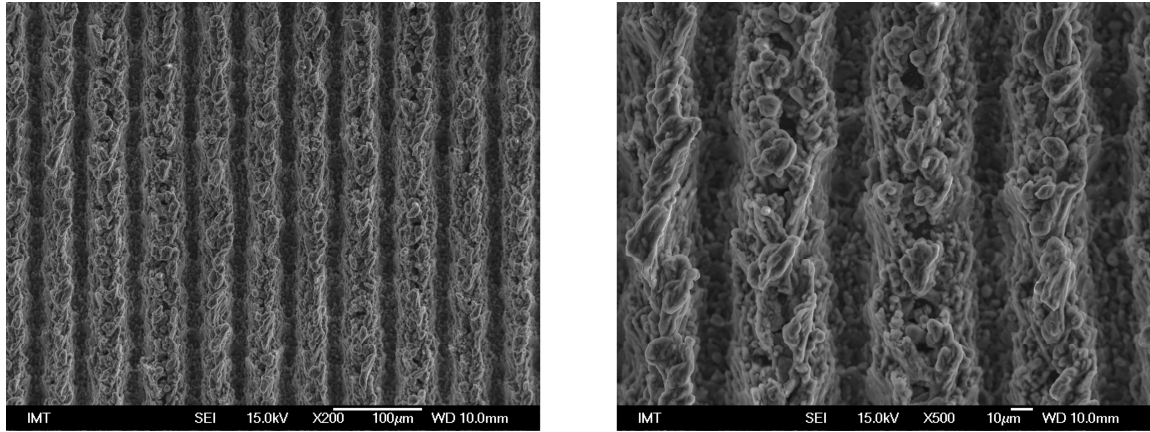
Figure S6. SEM images of the hydrophobized variable separation microcavity surface (HPO VS 3).
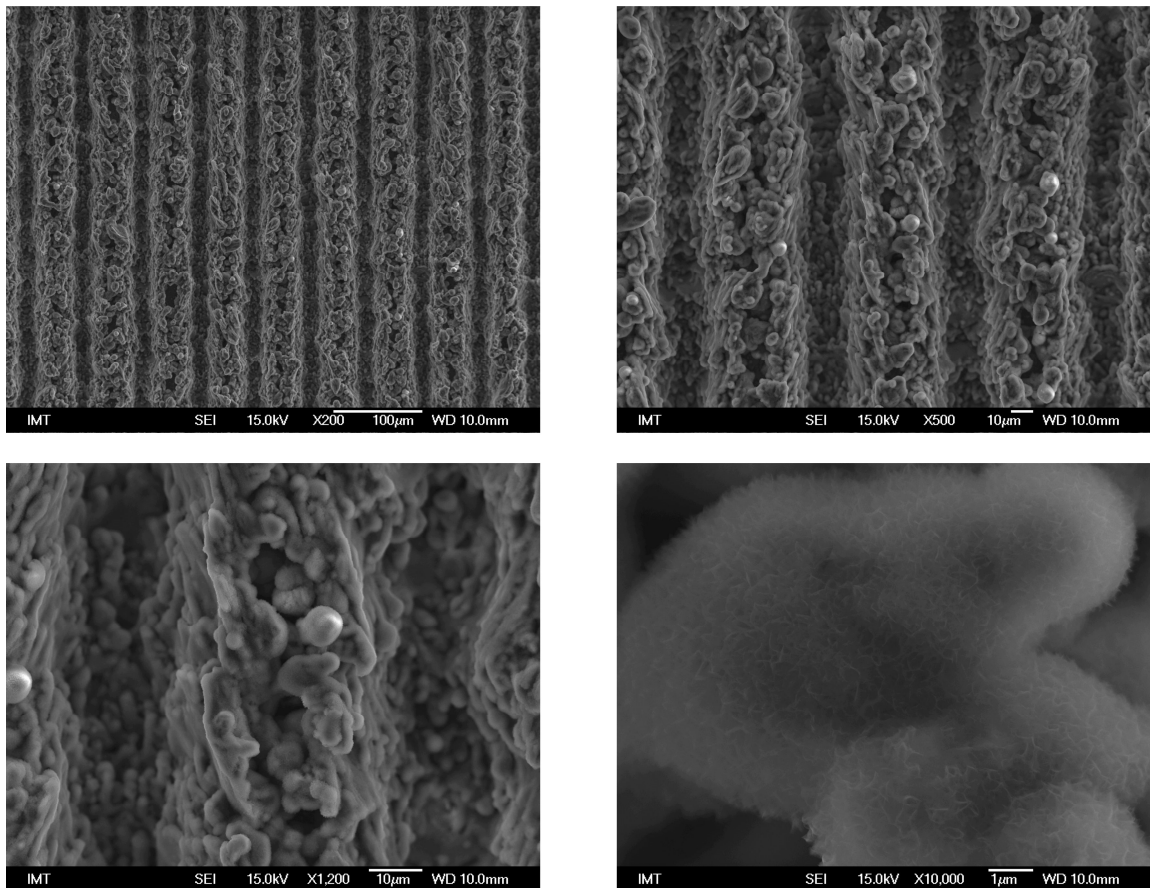
Figure S7. SEM images of the hydrophobized equidistant separation microcavity surface (HPO ES 1).
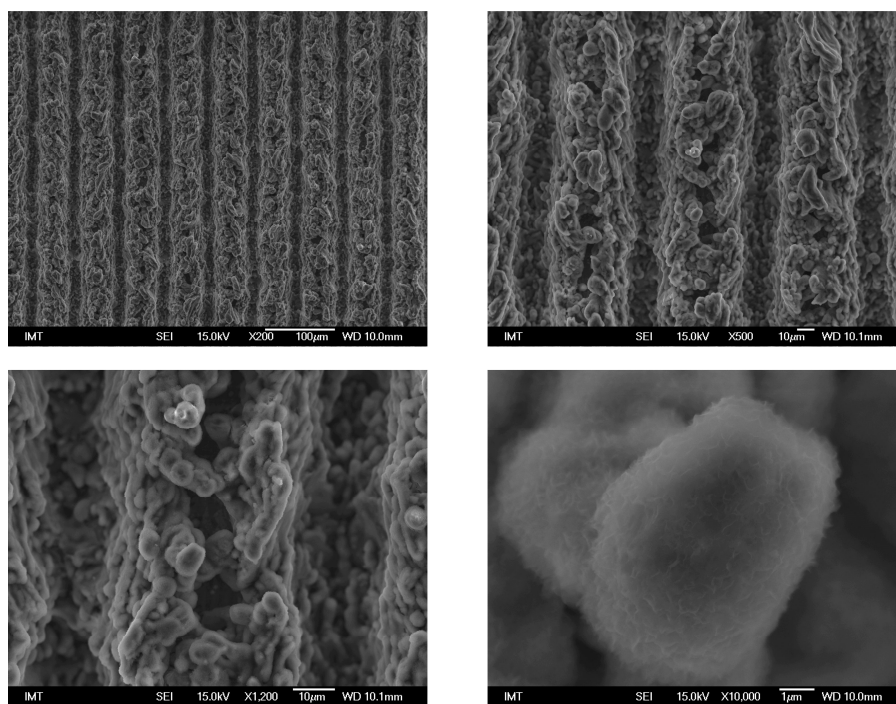
Figure S8. SEM images of the hydrophobized equidistant separation microcavity surface (HPO ES 2).
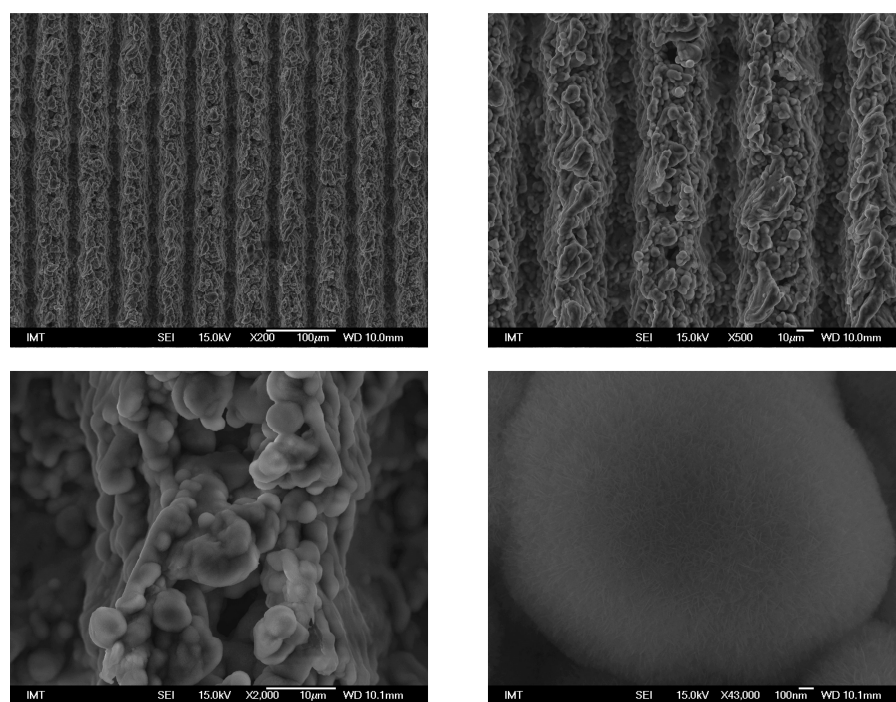
Figure S9. SEM images of the variable separation microcavity surface (HPI VS).
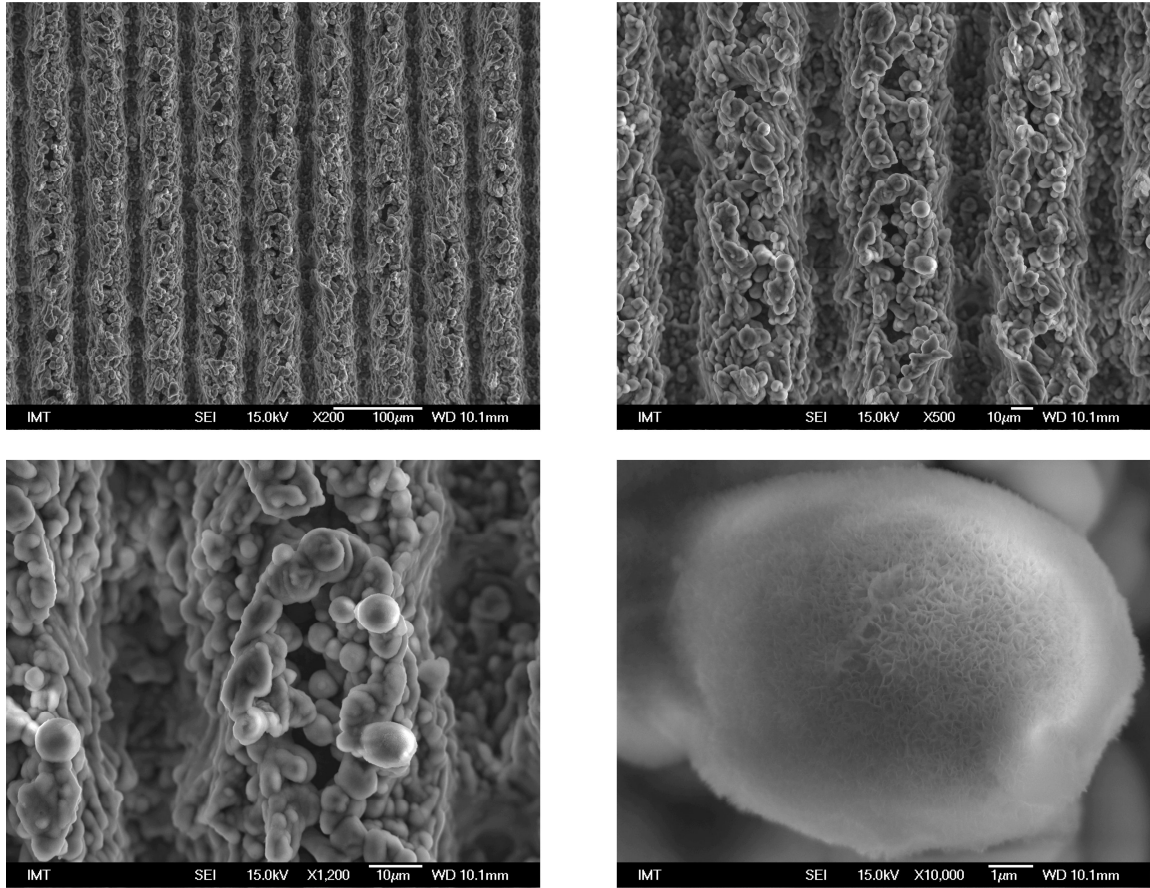
Figure S10. SEM images of the equidistant separation microcavity surface (HPI ES).

S2. FIB, SEM and EDS analysis of the oxide layer

Surface oxidation is inevitable when laser texturing a metal surface in an oxygen-containing atmosphere. The oxide layer was evaluated on cross sections of the samples HPO FT and HPI VS (**Figures S11-S12**). The cross sections were made by FIB milling using 30 keV Ga$^+$ ions. Since the angle between the SEM and the FIB columns equaled 54°, the vertical dimension scales as:

$$y_{real} = \frac{y_{SEM}}{\sin (54°)} \tag{S1}$$

To further confirm the presence of the oxide layer, 2D EDS mapping was performed as shown in **Figures S13-S16**. Note that the samples were coated by a 0.5 μm thick Pt layer before FIB milling. Oxygen was mapped to confirm the existence and the borders of the oxide layer. Fluorine was detected as it is contained in the HTMS coating, while aluminum, magnesium and silicon contents were mapped as they are the main alloying elements in the 6082 aluminum alloy (Table S1). The color denoting the concentration of an individual element progresses from black (no presence) through red towards yellow (high concentration).

According to Figure S13, oxygen is mainly present in the surface oxide layer and fluorine is present on the surface as a consequence of the HTMS coating. The layer of platinum used for surface protection during FIB milling is also clearly visible.

Similar results are also observable on Figure S14 (showing a different region on the same HPO FT sample cross section), where oxygen is primarily concentrated on the surface and in the oxide layer. It is also evident that the concentration of magnesium is uniform throughout the bulk of the cross section.

Figures S15 and S16 show the EDS analysis of FIB-made cross sections on the surface HPI VS. The cavity shown in Figure S15 has a high concentration of oxygen in the porous oxide layer, which is also sharply defined with no noticeable oxygen content gradient towards the bulk of the material.
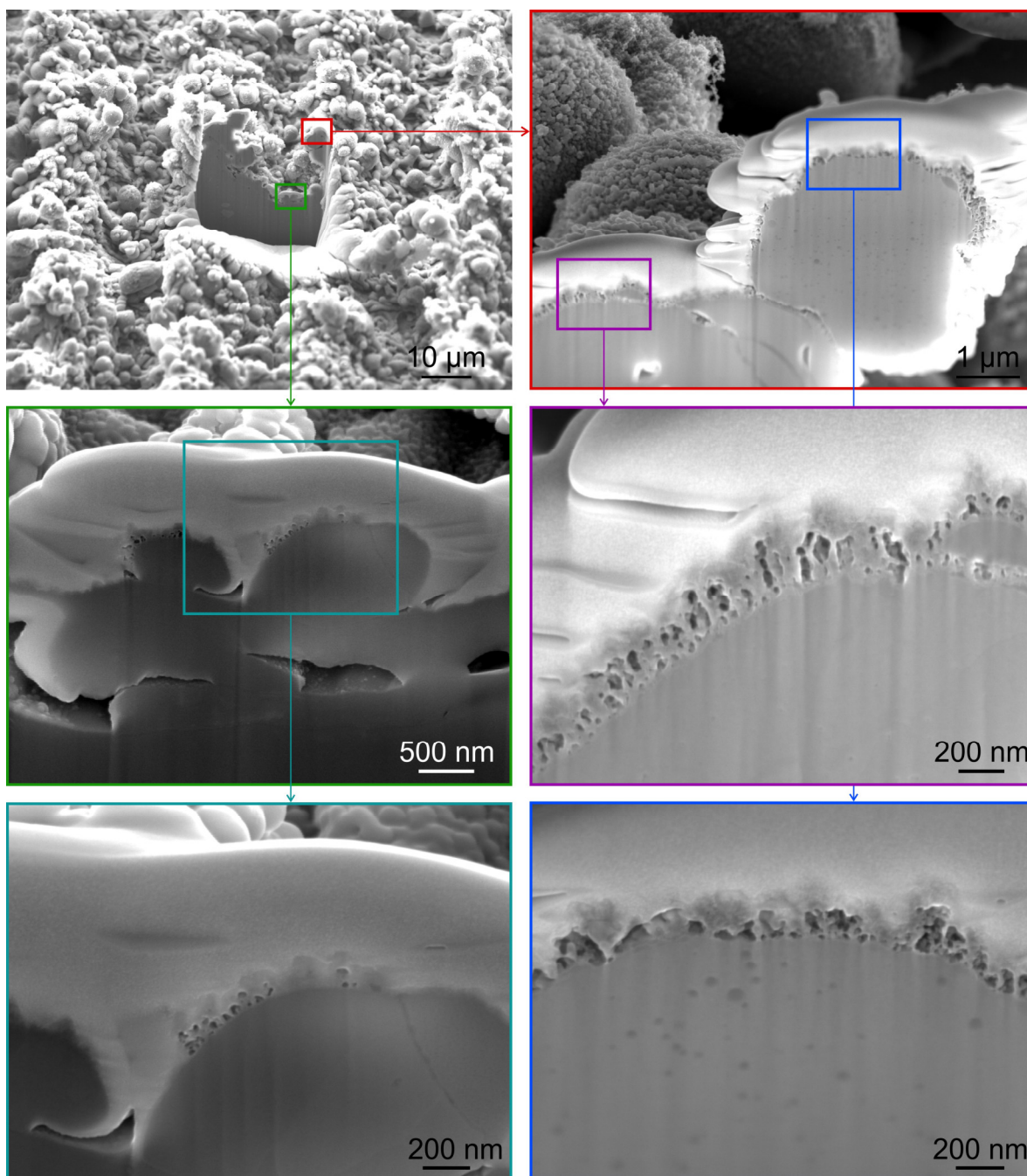
Figure S11. SEM images of a FIB cross section on the HPO FT surface.
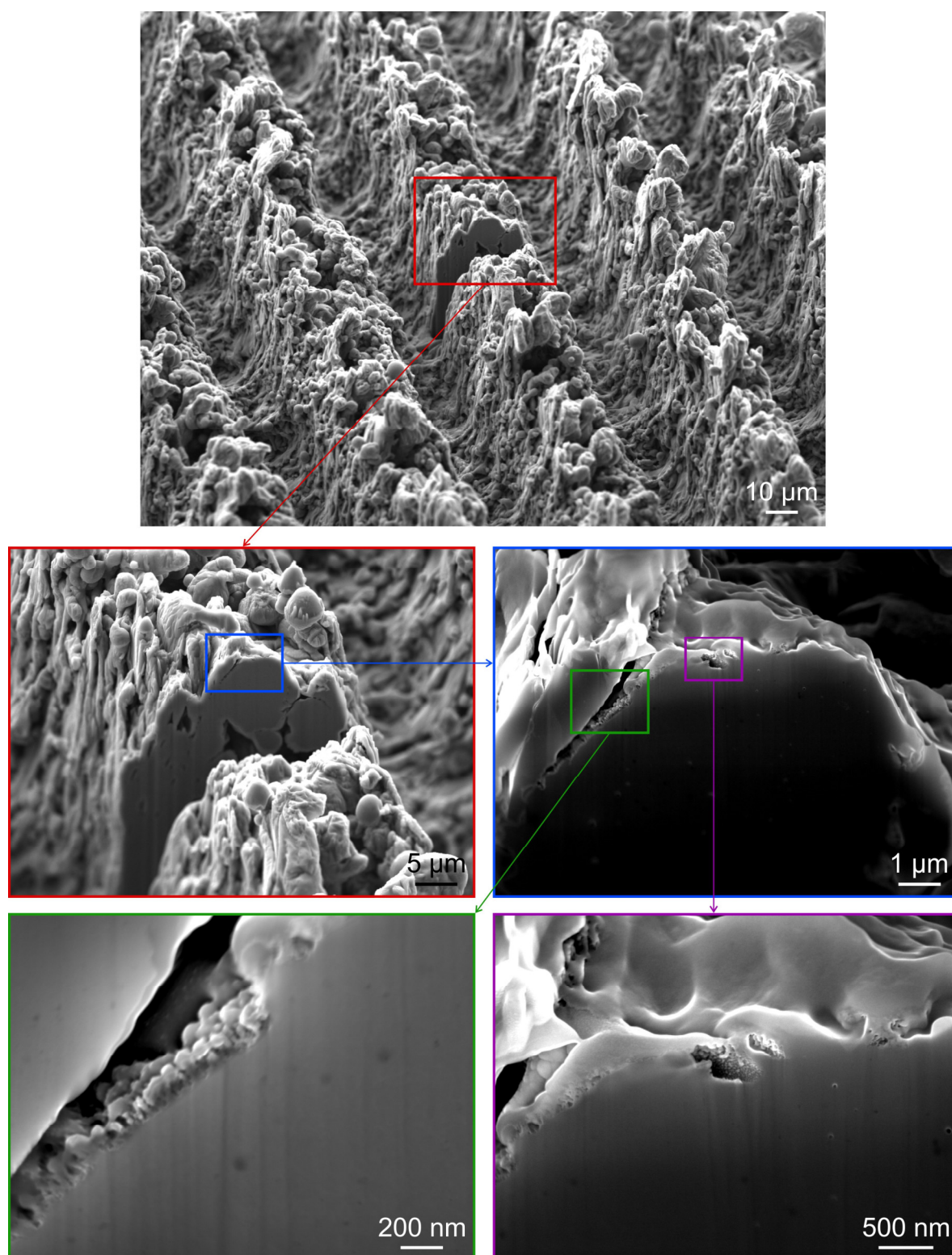
Figure S12. SEM images of a FIB cross section on the HPI VS surface.
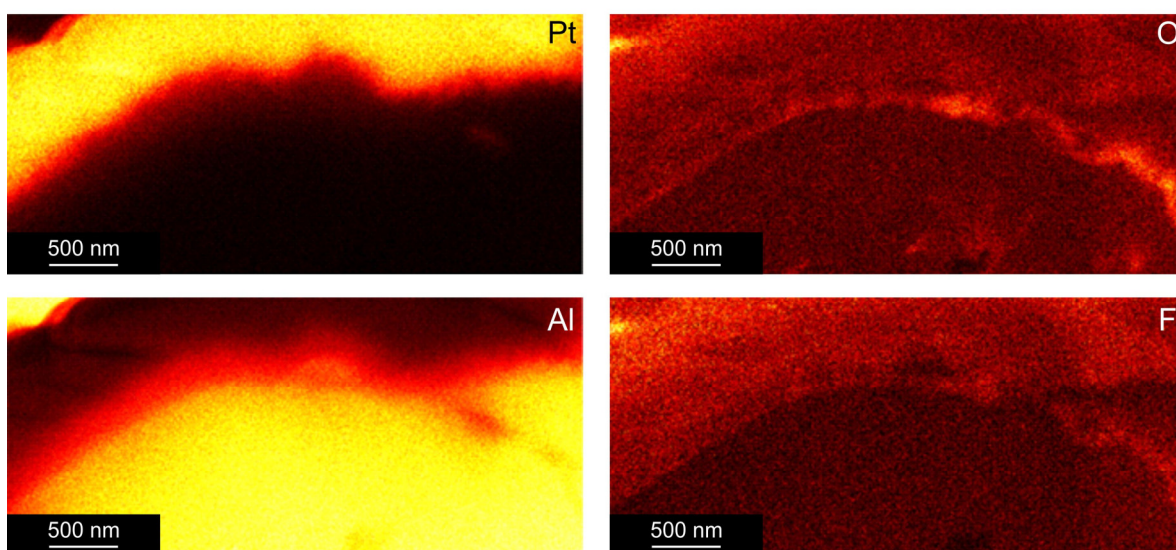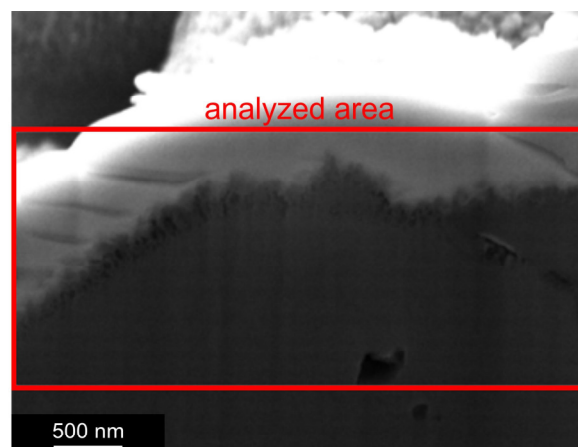
Figure S13. 2D EDS mapping of Pt, Al, O and F elements on the cross section of the surface HPO FT.
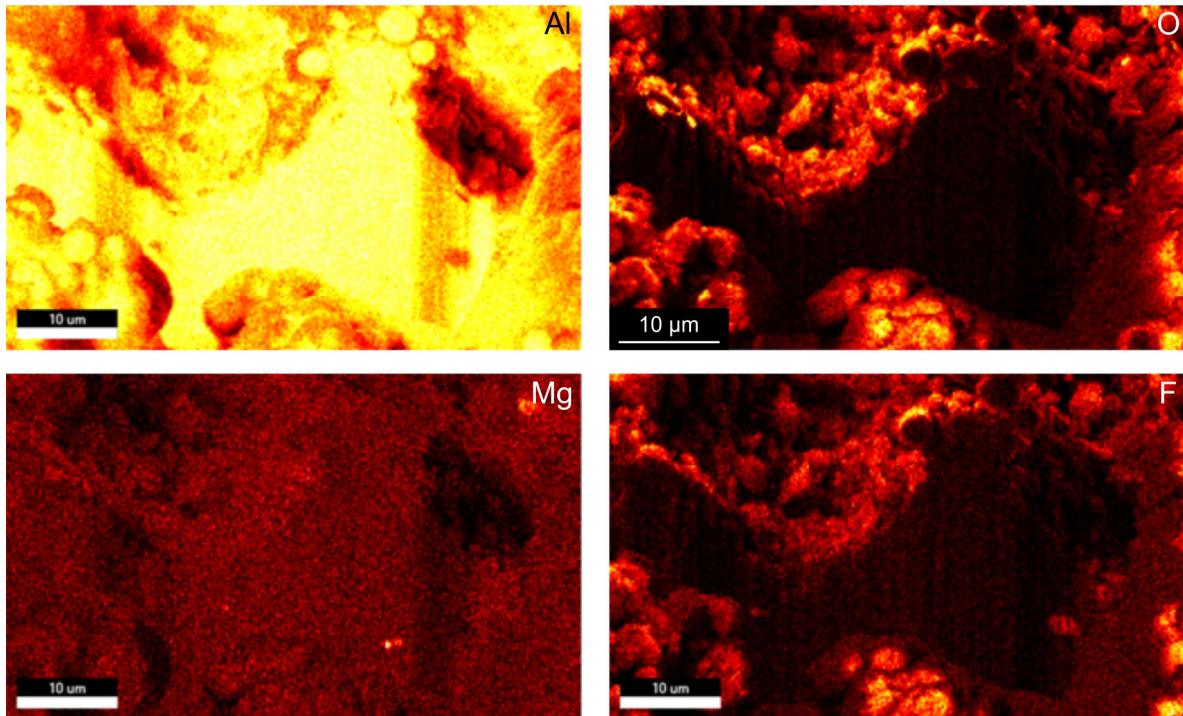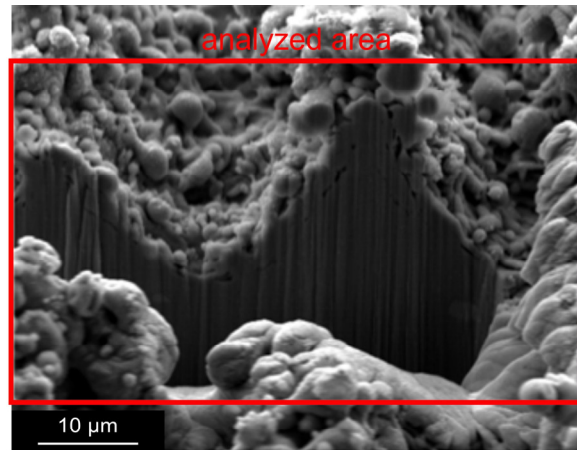
Figure S14. 2D EDS mapping of Al, O, Mg and F elements on the cross section of the surface HPO FT.
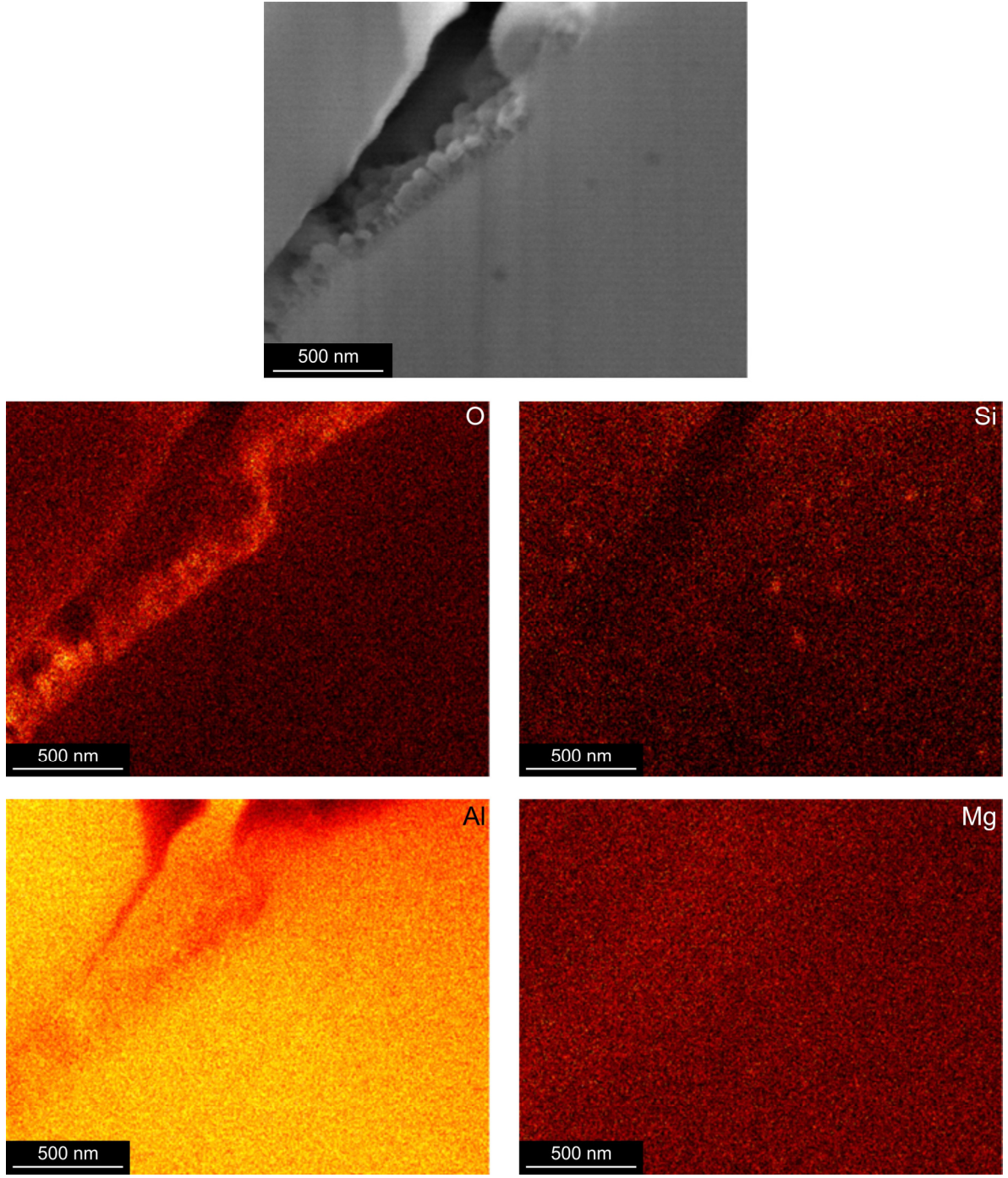
Figure S15. EDS analysis of O, Si, Al and Mg presence on the cross section of the surface HPI VS.
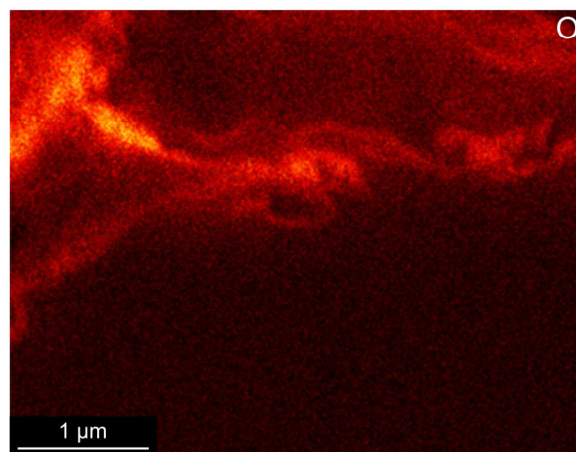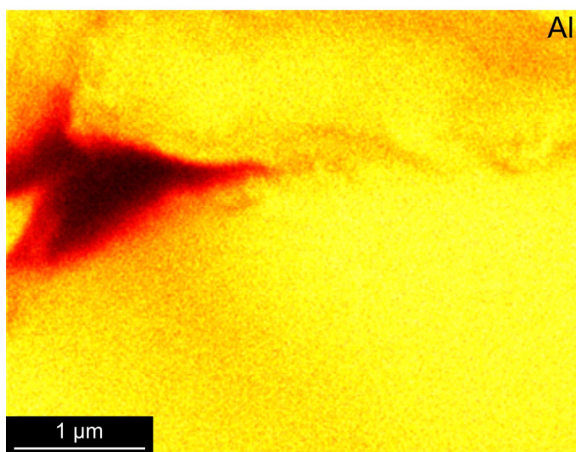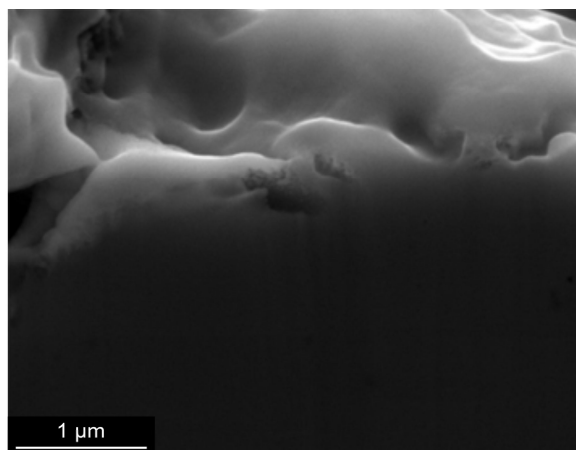
Figure S16. EDS analysis of O and Al presence on the cross section of the surface HPI VS.

Table S1. Chemical composition of 6082 aluminum according to the BS EN 573-3:2009 standard.

Element	Si	Mg	Mn	Fe	Cr	Zn	Ti	Cu	Al
Content in % wt.	0.7-1.3	0.6-1.2	0.4-1.0	< 0.5	< 0.25	< 0.2	< 0.1	< 0.1	balance

S3. Estimation of the temperature drop across the oxide layer

As shown by Kruse et al.[1], porous copper oxide can cause a deterioration of the heat transfer coefficient and the CHF during pool boiling. Furthermore, a low-thermal-conductivity layer can cause a significant increase in measurement uncertainty of the wall temperature and the surface superheat as shown in our previous publication.[2] According to existing studies[3,4], oxide layers induced by nanosecond laser texturing have a complex structure, which significantly depends on the laser fluence. Moreover, the boundary between the oxide and the substrate is often unclear, which makes it difficult to accurately perform composition analysis. Even though different oxide species can be formed during thermal treatment of aluminum and aluminum alloys,[3,5] Libenson et al.[6] clearly showed that aluminum is completely oxidized to Al_2O_3 during nanosecond laser treatment in the presence of atmospheric oxygen. Based on present results and literature review, we singled-out Al_2O_3 as the primary species in the oxide layer to evaluate the effect of the layer's thermal conductivity on surface temperature measurements.

A detailed analysis of FIB-SEM images (Figures S11-S12) revealed that the average thickness of the oxide layer equals ~410 nm and the void fraction was estimated as approx. 21% as presented in **Figure S17(a)**. Based on the literature-reported data[7–9], the thermal conductivity of Al_2O_3 oxide with near-zero porosity at 100 °C is around 30 W m^{-1} K^{-1}. Estimation of the porous oxide layer thermal conductivity can be done using the simple rule of mixtures:

$$k_{\text{porous layer}} = (k_{\text{Al2O3}} \cdot \omega_{\text{Al2O3}}) + (k_{\text{air}} \cdot \omega_{\text{air}}) \tag{S2}$$

where k is the thermal conductivity and ω is the volume fraction. Taking into account that thermal conductivity of (dry) air equals 0.316 W m^{-1} K^{-1} at 100 °C, the thermal conductivity of the porous oxide layer is estimated to be 23.8 W m^{-1} K^{-1}. This is considered as the best-case scenario.

On the other hand, the Al_2O_3 is not necessarily manifested as a single polycrystalline structure, but rather as a group of nanoparticles formed during nanosecond laser ablation. Nanostructure decreases the phonon mean free path and significantly reduces the thermal conductivity in comparison with the bulk value.[10] Braginsky et al.[11] measured and calculated the thermal conductivity of sintered porous Al_2O_3 nanostructures and obtained a thermal conductivity of 3.1 W m^{-1} K^{-1} at 100 °C for a sample with a 25% void fraction. This value is taken as the worst-

case scenario in our calculations. Based on these estimations and one-dimensional thermal conduction equation, we calculated the temperature drop through the oxide layer for three heat flux values relevant for our study.

Results presented in **Figure S17(b)** show that the maximum temperature drop across the porous oxide layer is below 0.2 K (at heat fluxes up to 1.5 MW m^{-2}), which is significantly lower than the measurement uncertainty of the wall temperature. For this reason, we do not account for this effect when extrapolating the surface temperature and calculating the surface superheat as it would only cause significant deviations if the oxide layer thickness was several micrometers or more.
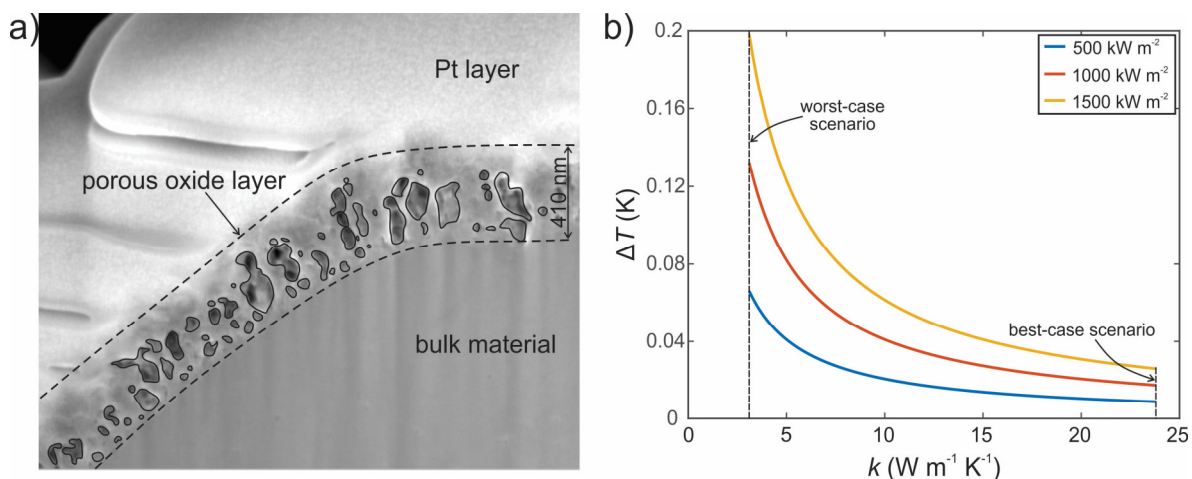
Figure S17. Porous oxide layer on a HPO FT surface (a) and temperature drop across the surface oxide layer versus its thermal conductivity at different heat fluxes (b).

S4. Laser-texturing strategy

Preliminary testing in combination with previous studies[2,12–16] was used to determine the appropriate parameters for microcavity formation. Laser texturing was performed using parallel scanning lines (0° texturing). The lateral separation between two consecutive scanning lines, i.e. the scanning line separation, was either kept constant or cycled within a certain range. Fully textured (FT) surfaces were treated using a constant separation of $\Delta y = 30$ μm, while equidistant separation (ES) microcavity surfaces were fabricated with a separation of $\Delta y = 65$ μm. Variable separation of $\Delta y = \{55$ μm, 60 μm, 65 μm$\}$ was used on the variable separation (VS) microcavity surfaces, where the separation increased and decreased in a cyclical fashion as shown in **Figure S18** and already explained by Gregorčič et al.[14]
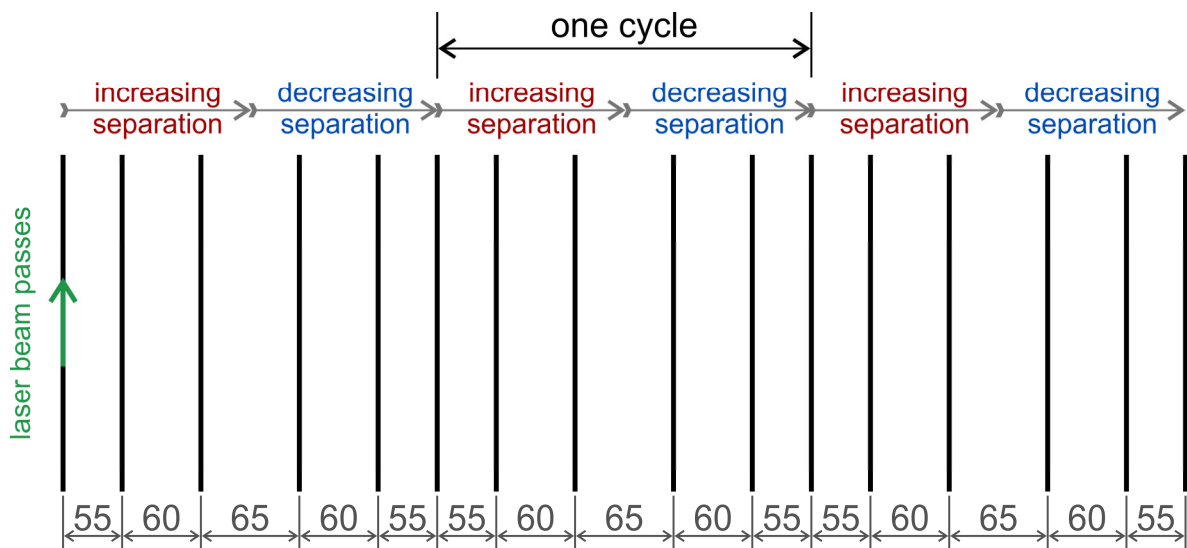
Figure S18. Schematic depiction of the variable separation concept; dimensions are in micrometers. The drawing is not to scale.

S5. Effect of scanning separation on microcavity formation

Scanning line separation between consecutive laser passes severely affects the formation of microcavities. Only a narrow range of separations will produce microcavities and within this range, different sizes of microcavities will appear. The optimal separation is a function of material properties and laser texturing parameters including the peak pulse fluence F_0, beam spot diameter and the consecutive pulse overlap δ (i.e., the combination of beam size, scanning velocity v, and pulse repetition rate). **Figure S19** shows the effect of scanning line separation on microcavity formation on 6082 aluminum alloy using the same texturing parameters that were later used to produce microcavity boiling surfaces for this study.

Figure S20(a) shows ridges with microcavities, formed due to laser irradiation, where the measured scanning line separation of consecutive laser beam passes was 55 μm or less. It can be observed that the ridges are narrow with overall smaller microcavities.

Figure S20(b) shows ridges with microcavities, where the measured scanning line separation of consecutive laser beam passes was 60 μm or more. It is evident that the ridges are wider compared to those in Figure S20(a) with a larger number of discernable microcavities, which also have a higher mean diameter.

$P = 17.8$ W; $F_0 = 17.3$ J cm^{-2}; $v = 400$ mm s^{-1};
$f = 180$ kHz; $\delta = 94$ %

laser beam passes

60 µm

25 µm

25 µm

100 µm
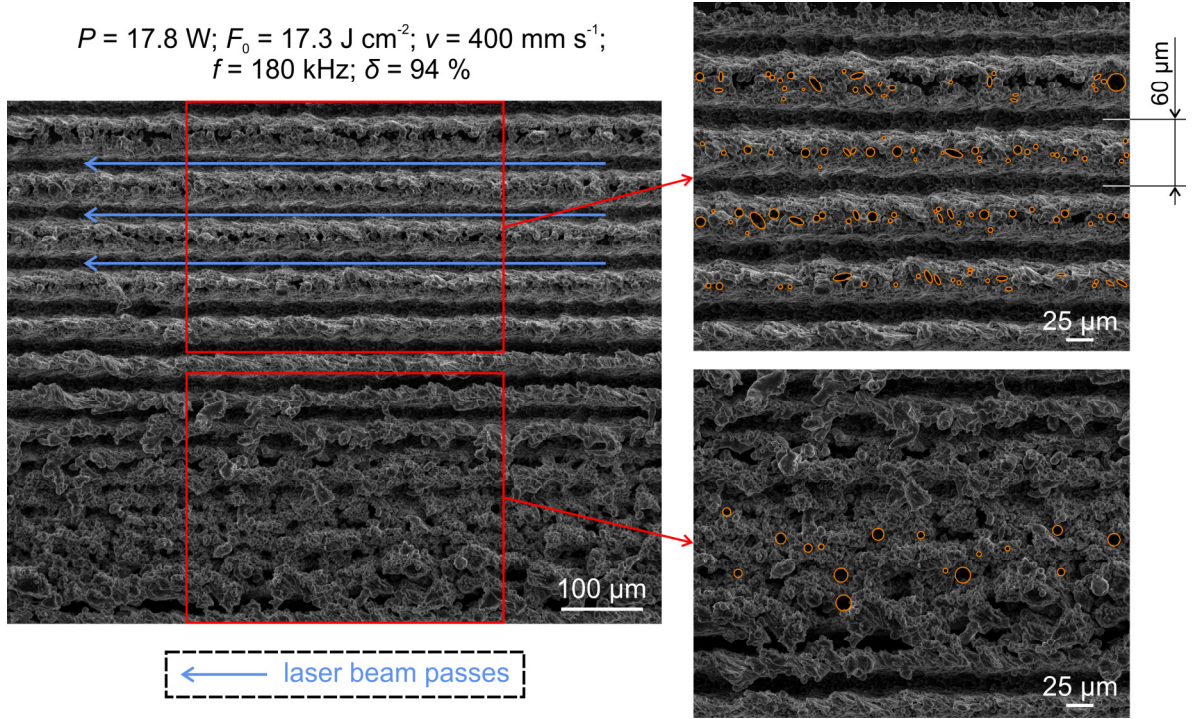
Figure S19. Influence of the laser scanning line separation on microcavity formation on the ridges between two consecutive laser beam passes. From top to bottom, scanning separation is being decreased by 5 µm per line from 65 µm to 15 µm.

(a)

(b)

50 µm
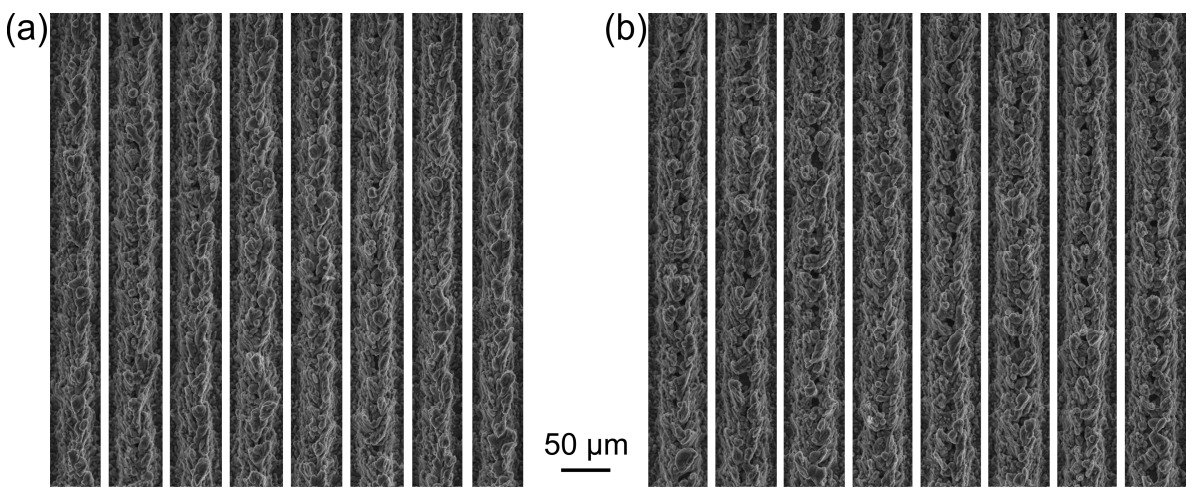
Figure S20. SEM images of ridges with microcavities created by a scanning line separation of under 55 µm (a) or over 60 µm (b).

S6. Dynamic contact angles on superhydrophobic surfaces

The advancing and receding contact angles (θ_a and θ_r, respectively) were evaluated on superhydrophobic surfaces using the droplet inflation/deflation method by inflating and deflating a water droplet at room temperature. Images taken by a high-speed camera were used to determine the values of the dynamic contact angles and the contact angle hysteresis (CAH) was calculated as the difference between the advancing and the receding contact angle. The recorded values including the standard deviation are listed in **Table S2**.

Table S2. Dynamic contact angles on superhydrophobic samples with corresponding standard deviation.

Sample	$\theta_a \pm \sigma(\theta_a)$ (°)	$\theta_r \pm \sigma(\theta_r)$ (°)	CAH $\pm \sigma$(CAH) (°)
HPO FT	159.8 ± 1.3	156.1 ± 1.9	3.7 ± 2.2
HPO ES	159.7 ± 2.0	155.1 ± 2.3	4.6 ± 2.9
HPO VS	159.6 ± 2.1	154.9 ± 1.7	4.7 ± 2.6

S7. Gas entrapment in surface cavities

On real (i.e., not smooth) surfaces the bubbles form during nucleate boiling via heterogeneous nucleation primarily from cavities on the surface. The geometry of the latter influences the wettability of the surface, the superheat required for the onset of nucleate boiling and the density of active nucleation sites. When a system, in which boiling is supposed to take place, is filled with the working fluid, the cavities on the surface can be filled with the liquid phase or air can be entrapped in them. Bankoff[17] assumed that gas will be entrapped in the cavity only if the angle of the cavity β is lower than the advancing contact angle:

$$\theta_a \geq \beta \tag{S3}$$

This phenomenon is shown in **Figure S21(a)**. During the growth of a vapor bubble from a cavity with a mouth diameter of r_c [shown in **Figure S21(b)**], the bubble will pass a critical growth phase, where the distance from its peak to the surface is b_2 and its radius is the smallest possible. From this it follows that the highest amount of energy (i.e., the largest superheat) is required to continue the bubble growth. This is called the critical hemispherical state and the required superheat for the continuation of bubble growth can be calculated from the following equation:

$$r = \frac{2\sigma T_{sat} v_g}{h_{fg} \Delta T_{sat}} \tag{S4}$$
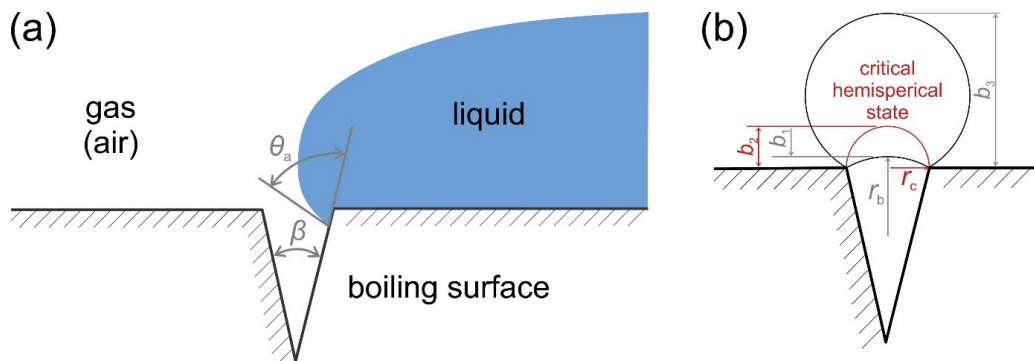
Figure S21. Entrapment of gas (air) into a cavity (a) and growth of a bubble from a conical cavity with shown critical hemispherical state (b).

S8. Comparison of boiling performance for all surfaces

Boiling curves (and with that, boiling performance) of all tested surfaces are compared in **Figure S22**. The magnitude of enhancement of HPO ES and HPO VS surfaces over other surfaces is clearly evident from the steep boiling curves, enhanced CHF values and low surface superheats throughout the entire nucleate boiling regime.
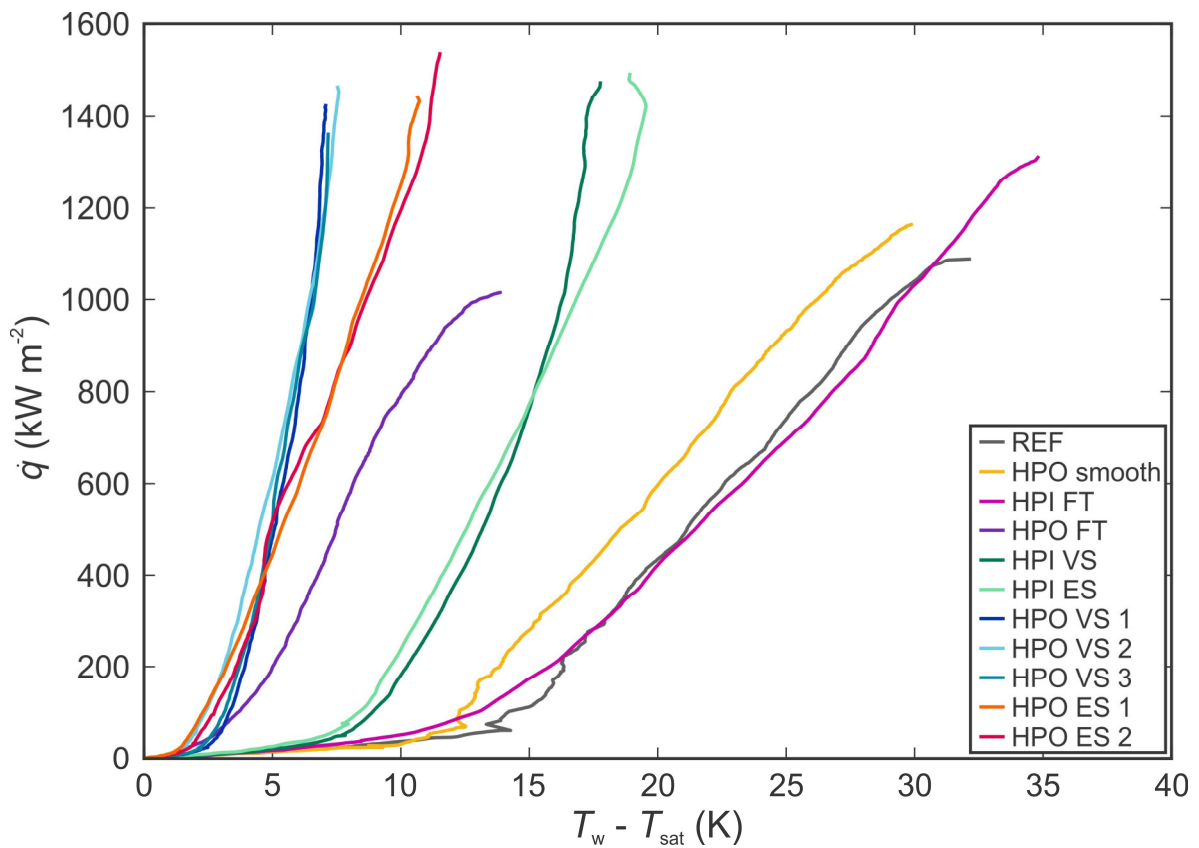
Figure S22. Comparison of boiling curves for all tested surfaces.

S9. Surface stability

Stability of superhydrophobic surfaces was investigated by repeated boiling performance tests. **Figure S23** shows the comparison of the boiling curves recorded during repeated pool-boiling runs on three surfaces.
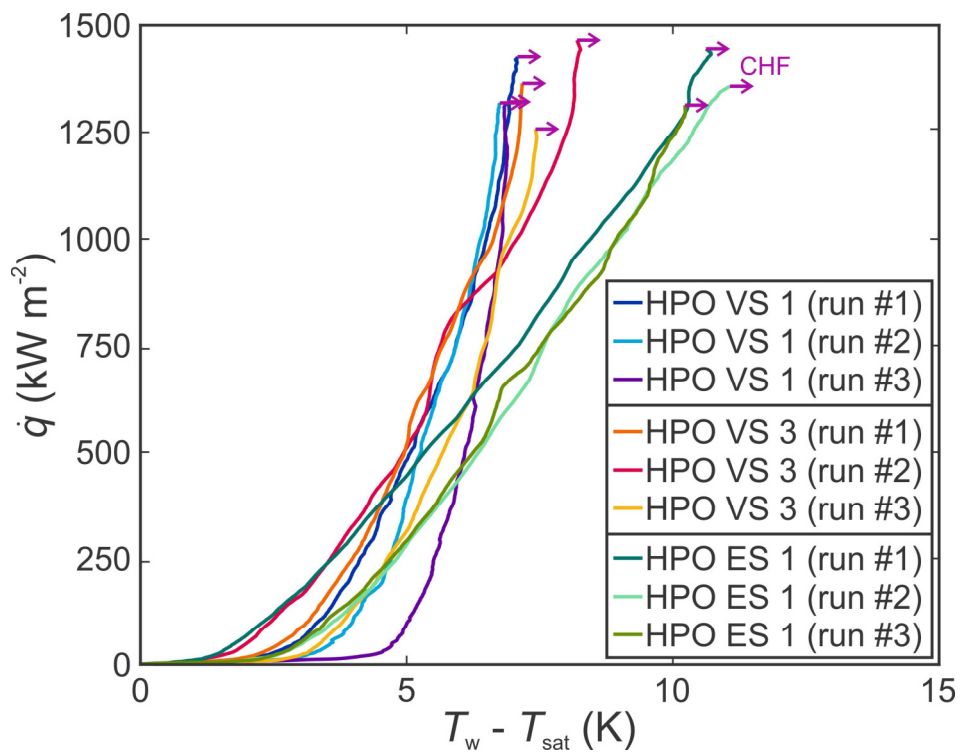
Figure S23. Evaluation of surface stability through repeated boiling tests on hydrophobized surfaces HPO VS 1, HPO VS 3 and HPO ES 1.

S10. Experimental setup

A schematic depiction of the pool boiling experimental setup is shown in **Figure S24**. The boiling chamber is constructed of a glass cylinder with an internal diameter of 100 mm between two stainless steel plates. An outer glass cylinder is used to limit air movement around the boiling chamber and thus the heat losses. Produced vapor is condensed in a glass condenser, which is also vented to the atmosphere to prevent the pressure from rising above atmospheric pressure. An immersion heater is installed in the chamber to preheat the working fluid up to the saturation temperature and to degas it prior to the start of measurements.

The heater assembly (shown in **Figure S25**) is inserted through the lower flange. A copper heating block is used to supply the heat from cartridge heaters in its base to the sample, which is positioned on top of it. Four thermocouples at a distance of 5 mm from one another are used to record the axial spatial temperature gradient in the heating stem, which is then used to calculate the heat flux. Since the copper stem is well insulated, the heat losses are negligible.

Figure S26 shows the data acquisition part of the experimental setup. A multiplexer module in a data logger switch unit is used to measure temperatures, which are then recorded and analyzed in LabVIEW environment running on a laptop computer.
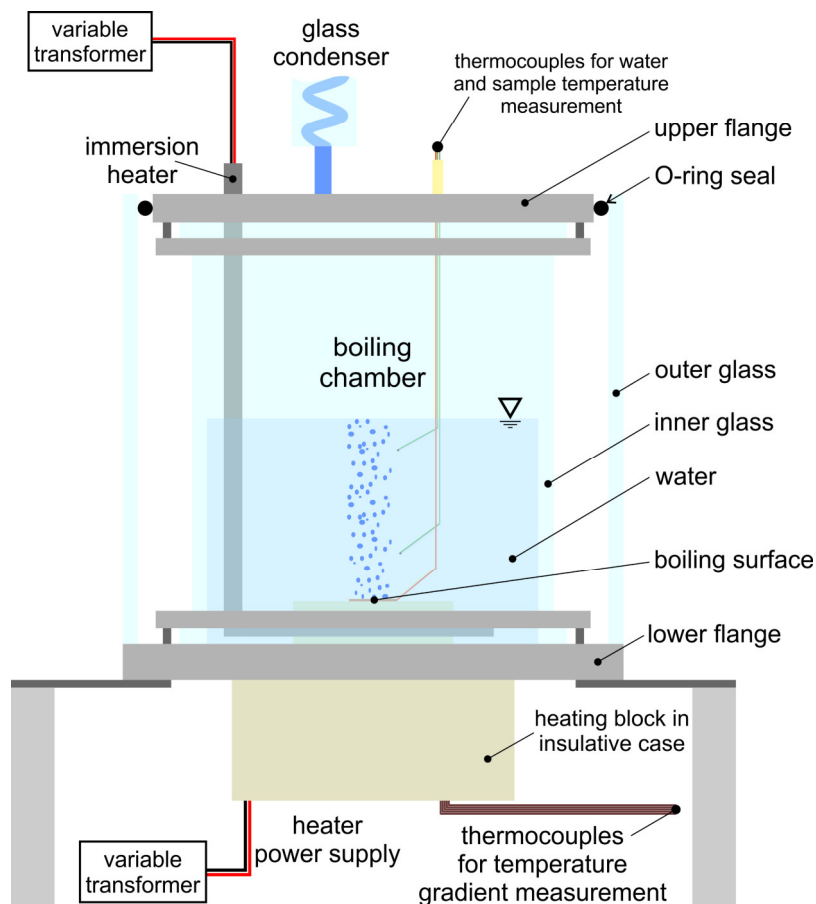
Figure S24. Schematic depiction of the experimental setup for boiling performance measurement.
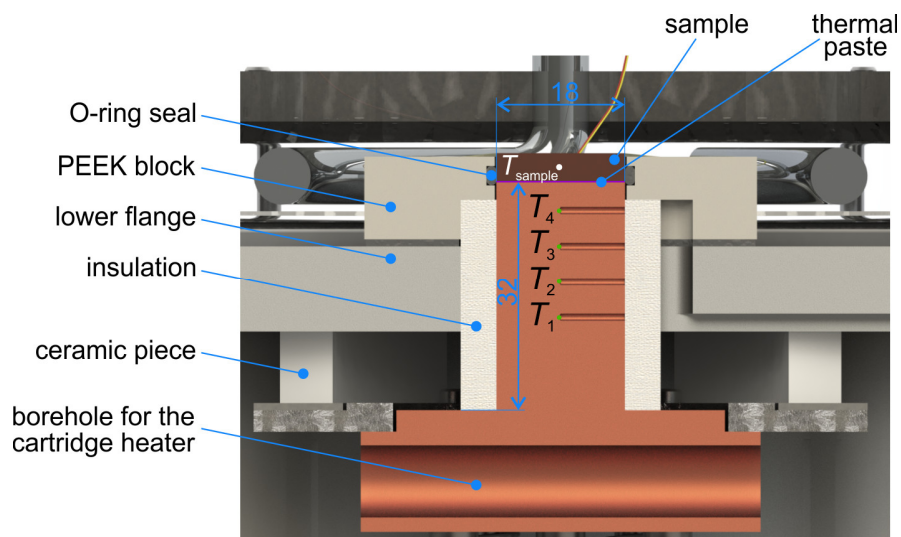
Figure S25. Cross section of the heater assembly part of the experimental setup.
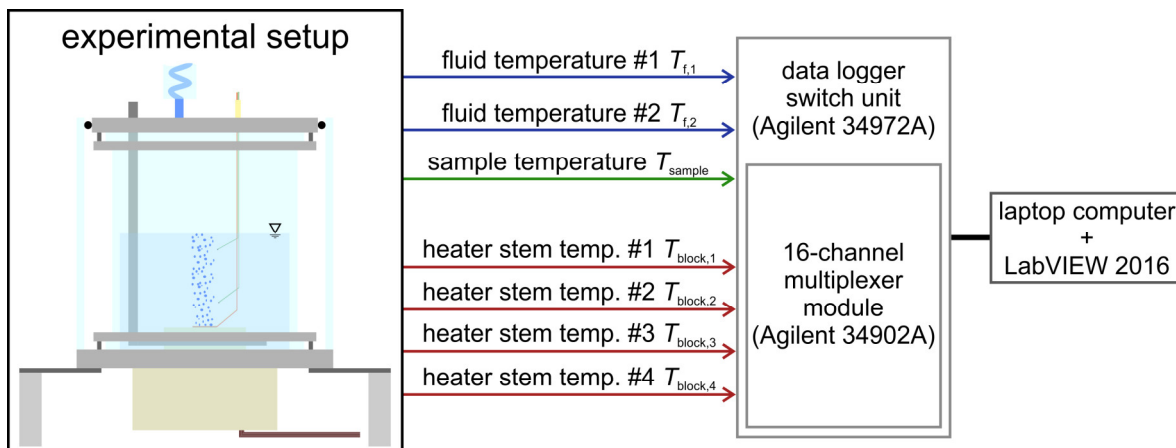
Figure S26. Schematic depiction of the data acquisition part of the experimental setup.

S11. Validation of the dynamic measurement approach

Measurements were performed using a dynamic measurement method where the heat flux was slowly but continuously increased by increasing the voltage supplied to the cartridge heaters in the heating block. The heat flux was raised by approx. 0.2 kW m^{-2} s^{-1} in the natural convection regime and up to approx. 2 kW m^{-2} s^{-1} in the nucleate boiling regime. This has the potential to cause deviations from true and accurate results due to thermal capacitance of the system (especially the heating block). Consequently, a validation experiment was performed to compare experimental results of steady state and dynamic measurements during one of our previous studies.[13] A total of four successive dynamic measurements were performed to record four boiling curves. An additional experimental run followed suit where the system was left to stabilize at 5 distinct heater powers; after a steady state was reached, the results were collected and averaged for 10 minutes. As it is evident from **Figure S27**, the steady state measurement points do not differ from the boiling curves recorded using a dynamic approach; any deviations are well within the measurement uncertainty.

The 1D heat transfer in the heating stem (and the sample) can also be analyzed using the simplified unsteady conduction equation along the x dimension accounting for the time t, temperature T and thermal diffusivity a:

$$\frac{\partial^2 T}{\partial x^2} = \frac{1}{a}\frac{\partial T}{\partial t}$$
(S5)

The thermal diffusivity is defined as the ratio between the thermal conductivity k and the product of specific heat c_p and density ρ:

$$a = \frac{k}{c_\mathrm{p}\rho}$$
(S6)

It can be concluded from Eq. (S5) that high values of the thermal diffusivity allow for reasonable temporal temperature gradients (e.g., heating rates) while keeping the spatial temperature gradients fairly linear (and with that, the spatial distribution of the heat flux nearly uniform). Thermal diffusivity of copper (~1.1 mm^2 s^{-1}) and aluminum (~0.81 mm^2 s^{-1}) is much higher than that of

stainless steel for example (~0.03-0.04 mm^2 s^{-1}), making unsteady heating as an approximation of steady-state measurements viable.

Furthermore, it has been shown by a number of researchers[13,18–20] that the surfaces change over time during exposure to the boiling process. This is especially true when using water as the working fluid since it typically reacts with the surface to form oxides or similar compounds, which can change the wettability and the morphology of the surface, both of which impact the boiling process. Therefore, performing a boiling curve measurement over a prolonged period (e.g., 8 hours) to record many steady states might result in measurement errors since the surface is not the same after several hours of water immersion and exposure to boiling. It could even be said that in such cases, the boiling process is being observed on a slightly different surface as time goes by. This makes dynamic measurements where the boiling curve is recorded within approx. 30 min especially viable in evaluating the performance of the surface at a given moment in time.

A detailed heating rate analysis was performed in QuickField 6.3 environment, where an axisymmetric model of the heating stem and the sample was built. The following material properties were used in the simulation: thermal conductivity of 365 W m^{-1} K^{-1} for copper and 200 W m^{-1} K^{-1} for aluminum, specific heat capacity of 385 J kg^{-1} K^{-1} for copper and 920 J kg^{-1} K^{-1} for aluminum, density of 8960 kg m^{-3} for copper and 2700 kg m^{-3} for aluminum. Temperature-dependent values were not used to keep the analysis simple and since their use would not impact the results in a meaningful way. Thermal interface between the copper steam and the aluminum sample was not considered since it has negligible thermal capacitance due to its thinness and would not impact the results of the analysis. A linearly increasing heat input from 0 to 500 kW m^{-2} was simulated at the bottom of the heating stem and heat flux values were monitored at specific nodes of the mesh. The results are normalized to give a clearer picture of the heat flux gradients. The simulations were repeated at a maximum heat fluxes of 100 kW m^{-2} and 1 MW m^{-2}. It was established that the normalized values do not change. Heat losses were considered negligible in the same way as during the calculation of the heat flux based on spatial temperature gradient measurement. While some minor losses are inevitable, they are also present during steady state measurements where they have the potential to induce a heat flux gradient. Therefore, accounting for them would possibly obscure the actual influence of the heating rate on the spatial distribution of the heat flux.

The results of the heating rate analysis are shown in **Figure S28** and **Table S3**. For very slow heating rates of below 1 kW m^{-2} s^{1}, the heat flux gradient in the stem and the sample will be hardly noticeable. If the heating rate is increased, the gradient will be more pronounced and a heat flux difference of more than 20% between the left and the right side of the heating system in Figure S28 will be present at heating rates above 5 kW m^{-2} s^{-1}.

The normalized results in Table S3 show the heat flux $\dot{q}_{\mathrm{meas,norm}}$, that would be measured based on the spatial temperature gradient recorded by four thermocouples in the heating steam. In this analysis, it is estimated as the arithmetic average of the heat flux at the leftmost and the rightmost thermocouple in the copper heating stem in Figure S28, the geometry of which matches that of the experimental setup used in our pool boiling measurements. The normalized heat flux actually present at the surface is denoted as $\dot{q}_{\mathrm{surf,norm}}$. It is evident that the "measured" heat flux is significantly lower than that present at the leftmost thermocouple for high heating rates (≥ 5 kW m^{-2} s^{-1}). Furthermore, a difference between the heat flux present at the boiling surface and the "measured" heat flux also increases with increasing heating rate with the relative differences given in the rightmost column of Table S3. Based on these results, we estimate that the 4.6% difference obtained at a heating rate of 2 kW m^{-2} s^{-1} is still acceptable since it is lower than the relative measurement uncertainty of the heat flux measurements (10.5% at 100 kW m^{-2} and 5.3% at 1 MW m^{-2}).
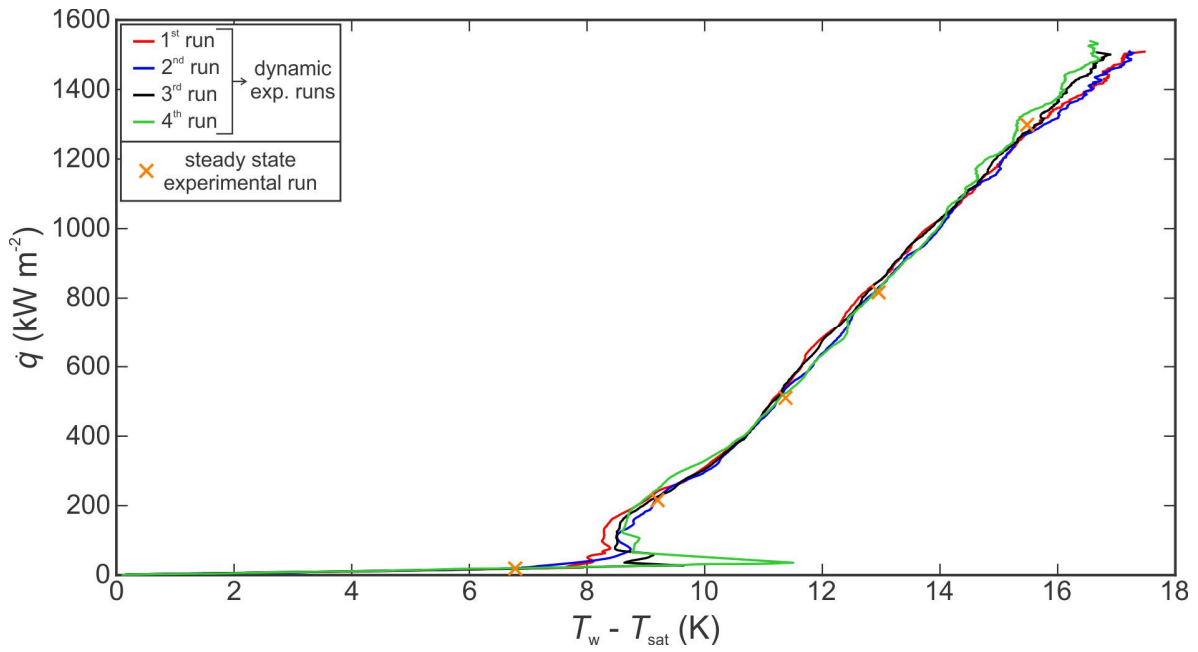
Figure S27. Validation of dynamic boiling heat transfer performance measurement.
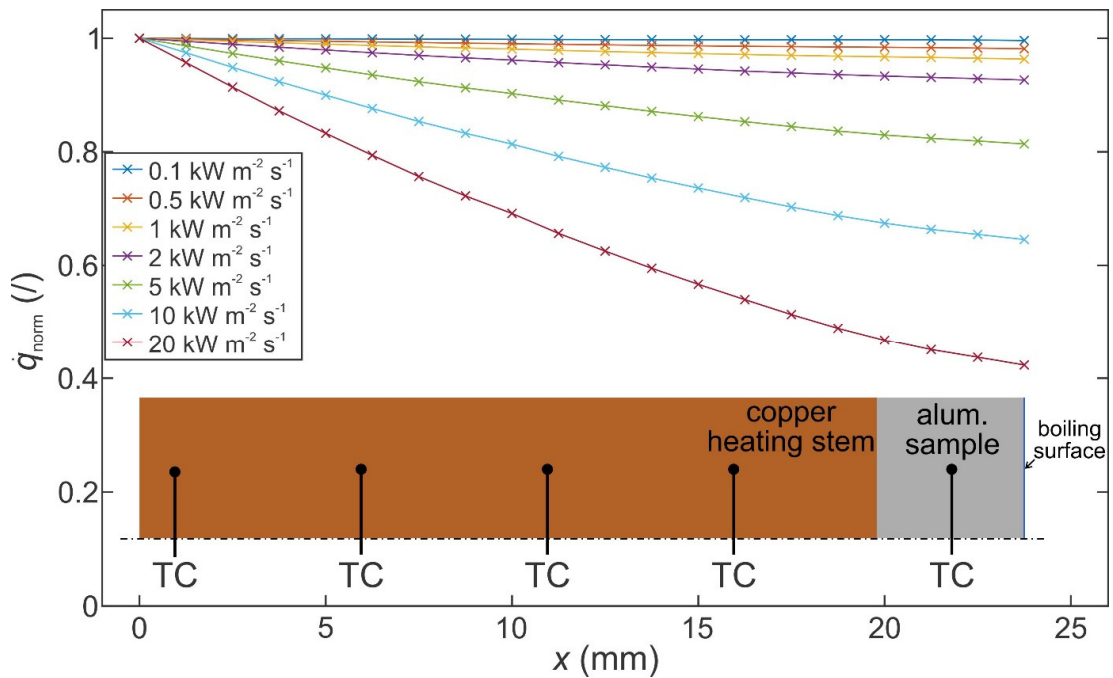
Figure S28. Normalized heat flux versus axial distance along the copper heating stem and the aluminum sample for different heating rates. The inset stem drawing is not to scale.

Table S3. Normalized measured "average" heat flux between the thermocouples in the copper stem and normalized actual heat flux at the boiling surface.

Heating rate (kW m^{-2} s^{-1})	$\dot{q}_{meas,norm}$ (/)	$\dot{q}_{surf,norm}$ (/)	$\Delta\dot{q}$ (%)
0.1	0.999	0.996	-0.2
0.5	0.993	0.982	-1.1
1	0.986	0.963	-2.3
2	0.971	0.927	-4.6
5	0.927	0.814	-12.2
10	0.860	0.646	-24.9
20	0.768	0.423	-44.9

S12. Effect of working fluid degassing

A film of air was observed on all superhydrophobic samples immediately after immersion in water. The film gradually disappeared during the degassing process using immersion heaters with the surface transitioning into the initial Wenzel wetting state prior to the boiling experiments in the same way as described by Allred et al.[21] To test how degassing of the working fluid affects the results of boiling performance measurements, an additional measurement was conducted using the fully superhydrophobic surface HPO FT. Instead of usual degassing of the working fluid (water) though vigorous boiling for 60 minutes using the immersion heater, the degassing process was reduced to 5 minutes of boiling after saturation temperature was reached. A boiling curve measurement was then performed. As it is evident from **Figure S29**, the boiling curve for improperly degassed working fluid is completely different than the boiling curved obtained under degassed conditions, where the surface is in the initial Wenzel wetting state. Without proper degassing, the surface becomes covered by a vapor film immediately as the boiling measurement starts and gradually transitions towards film boiling with a CHF barely above 200 kW m^{-2}.
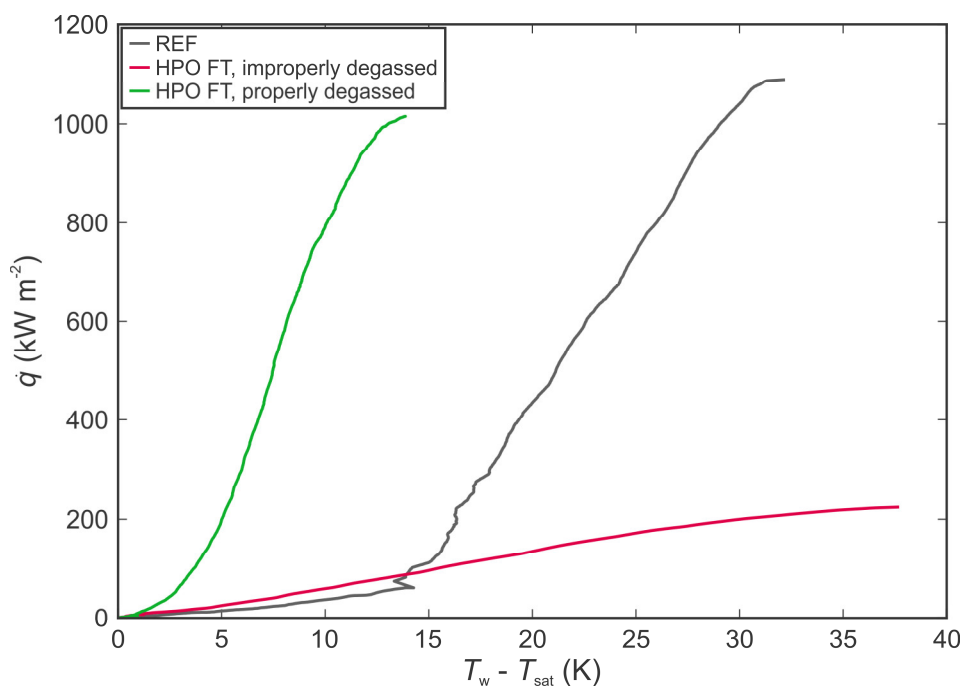
Figure S29. Evaluation of the effect of proper working fluid degassing on surface HPO FT.

S13. Data reduction and measurement uncertainty calculation

13.1 Data reduction

Four temperatures recorded in the heating stem are used to calculate the spatial temperature gradient:

$$\frac{\Delta T}{\Delta x} = \frac{\frac{T_1 - T_3}{2\Delta x} + \frac{T_2 - T_4}{2\Delta x}}{2} = \frac{T_1 + T_2 - T_3 - T_4}{4\Delta x} \tag{S7}$$

where T_1, T_2, T_3 and T_4 are the measure temperatures from Figure S25 and Δx is the distance between two adjacent thermocouples (5 mm). The spatial temperature gradient is then used to calculate the heat flux in the heating stem:

$$\dot{q} = k_{Cu} \frac{\Delta T}{\Delta x} \tag{S8}$$

where k_{Cu} is the temperature dependent thermal conductivity of copper. The latter was determined by measuring the thermal diffusivity of copper samples and calculating the thermal conductivity using literature data for the specific heat capacity and density. The following equation is used to describe the thermal conductivity of copper:

$$k_{Cu}(T) = 0.000283T^2 - 0.1646T + 378.07 \tag{S9}$$

Temperature is inserted in degrees Celsius and the resulting thermal conductivity is expressed in W m^{-1} K^{-1}. The temperature of the surface is calculated by assuming the heat flux in the stem is the same as in the sample. The following equation is used:

$$T_{surface} = T_{sample} - \frac{\dot{q}\Delta x_2}{k_{Al}} \tag{S10}$$

where T_{sample} is the temperature measured in the middle of the sample, Δx_2 is the distance from the thermocouple in the sample to the boiling surface (2 mm) and k_{Al} is the temperature dependent thermal conductivity of aluminum.

The latter is evaluated the same way as for copper and given by the following equation:

$$k_{Al}(T) = -0.0001165T^2 + 0.07486T + 198.81 \tag{S11}$$

The surface superheat is calculated by subtracting the average water temperature from the temperature of the surface:

$$T_w - T_{sat} = T_{surface} - \frac{T_{water,1} + T_{water,2}}{2} \tag{S12}$$

Finally, the heat transfer coefficient is calculated by dividing the heat flux by the surface superheat:

$$h = \frac{\dot{q}}{T_w - T_{sat}} \tag{S13}$$

13.2 Measurement uncertainty

Measurement uncertainty was evaluated using the uncertainties of contributing parameters listed in **Table S4**. The uncertainty evaluation was conducted in accordance with the method described by Može et al.[22]

The uncertainty of the distance between two thermocouples is affected by the uncertainty of position of each thermocouple; no correlation is assumed. Therefore, combined distance uncertainty is:

$$u(\Delta x_1) = \sqrt{2\left(\frac{u_{TC}}{\sqrt{3}}\right)^2 + 2\left(\frac{u_{hole}}{\sqrt{3}}\right)^2} = 0.25 \text{ mm} \tag{S14}$$

The uncertainty of the distance from the thermocouple in the sample to the boiling surface is only affected by the uncertainty of one thermocouple hole and the position of the thermocouple in this hole:

$$u(\Delta x_2) = \sqrt{\left(\frac{u_{TC}}{\sqrt{3}}\right)^2 + \left(\frac{u_{hole}}{\sqrt{3}}\right)^2} = 0.18 \text{ mm} \tag{S15}$$

Uncertainty of the heat flux is calculated using the following equation:

$$u(\dot{q}) = \sqrt{\begin{array}{c} \left(\frac{\partial \dot{q}}{\partial T_1}\right)^2 u^2(T_1) + \left(\frac{\partial \dot{q}}{\partial T_2}\right)^2 u^2(T_2) + \left(\frac{\partial \dot{q}}{\partial T_3}\right)^2 u^2(T_3) + \left(\frac{\partial \dot{q}}{\partial T_4}\right)^2 u^2(T_4) + \\ + \left(\frac{\partial \dot{q}}{\partial k_{Cu}}\right)^2 u^2(k_{Cu}) + \left(\frac{\partial \dot{q}}{\partial \Delta x_1}\right)^2 u^2(\Delta x_1) \end{array}} \qquad (S16)$$

The latter equation needs to be evaluated for each measurement as its result depends on the actual temperatures present in the system during operation. At a low heat flux of 100 kW m^{-2}, the standard measurement uncertainty of heat flux is approx. 10.5 kW m^{-2} and at a high heat flux of 1000 kW m^{-2}, its value increases to approx. 53 kW m^{-2}.

The uncertainty of surface superheat is evaluated based on the uncertainties of the heat flux, the temperature in the sample and of the water, and the thermal conductivity:

$$u(T_w - T_{sat}) = \sqrt{\begin{array}{c} \left(\frac{\partial T_w - T_{sat}}{\partial T_{sample}}\right)^2 u^2(T_{sample}) + \left(\frac{\partial T_w - T_{sat}}{\partial T_{water}}\right)^2 u^2(T_{water}) + \\ \left(\frac{\partial T_w - T_{sat}}{\partial \Delta x_2}\right)^2 u^2(\Delta x_2) + + \left(\frac{\partial T_w - T_{sat}}{\partial \dot{q}}\right)^2 u^2(\dot{q}) + \left(\frac{\partial T_w - T_{sat}}{\partial k_{Al}}\right)^2 u^2(k_{Al}) + \end{array}} \qquad (S17)$$

The uncertainty of the heat transfer coefficient is calculated using the following equation:

$$u(h) = \sqrt{\left(\frac{\partial h}{\partial \dot{q}}\right)^2 u^2(\dot{q}) + \left(\frac{\partial h}{\partial T_w - T_{sat}}\right)^2 u^2(T_w - T_{sat})} \qquad (S19)$$

As with the heat flux uncertainty, surface superheat and heat transfer coefficient uncertainties need to be evaluated using actual measured data. Surface superheat uncertainty is approx. 0.38 K at 100 kW m^{-2} and 1.07 K at 1000 kW m^{-2}, whereas the uncertainty of the heat transfer coefficient is very dependent on the actual surface and can range between 0.19-3.4 kW m^{-2} K^{-1} at 100 kW m^{-2} and between 1.3-25.3 kW m^{-2} K^{-1} at 1000 kW m^{-2}.

Table S4. List of uncertainties of contributing parameters.

Uncertainty	Symbol	Type	Value
thermocouple hole position	u_{TC}	limit of error	0.3 mm
position of a thermocouple inside the hole	u_{hole}	limit of error	0.05 mm
thermocouple temperature measurement	u_{T}	standard	0.25 K
thermal conductivity determination	u_{k}	relative	1.5%

S14. References

(1)   Kruse, C.; Tsubaki, A.; Zuhlke, C.; Alexander, D.; Anderson, M.; Peng, E.; Shield, J.; Ndao, S.; Gogos, P. G. Influence of Copper Oxide on Femtosecond Laser Surface Processed Copper Pool Boiling Heat Transfer Surfaces. *J. Heat Transfer* **2019**, *141* (5), 1–9. https://doi.org/10.1115/1.4043129.

(2)   Zupančič, M.; Može, M.; Gregorčič, P.; Sitar, A.; Golobič, I. Evaluation of Enhanced Nucleate Boiling Performance through Wall-Temperature Distributions on PDMS-Silica Coated and Non-Coated Laser Textured Stainless Steel Surfaces. *Int. J. Heat Mass Transf.* **2017**, *111*, 419–428. https://doi.org/10.1016/j.ijheatmasstransfer.2017.03.128.

(3)   Mroczkowska, K. M.; Antończak, A. J.; Gąsiorek, J. The Corrosion Resistance of Aluminum Alloy Modified by Laser Radiation. *Coatings* **2019**, *9* (10), 672. https://doi.org/10.3390/coatings9100672.

(4)   Boinovich, L. B.; Emelyanenko, A. M.; Modestov, A. D.; Domantovsky, A. G.; Emelyanenko, K. A. Synergistic Effect of Superhydrophobicity and Oxidized Layers on Corrosion Resistance of Aluminum Alloy Surface Textured by Nanosecond Laser Treatment. *ACS Appl. Mater. Interfaces* **2015**, *7* (34), 19500–19508. https://doi.org/10.1021/acsami.5b06217.

(5)   Gleizes, A. N.; Vahlas, C.; Sovar, M. M.; Samélor, D.; Lafont, M. C. CVD-Fabricated Aluminum Oxide Coatings from Aluminum Tri-Iso-Propoxide: Correlation between Processing Conditions and Composition. *Chem. Vap. Depos.* **2007**, *13* (1), 23–29. https://doi.org/10.1002/cvde.200606532.

(6)   Libenson, M. N.; Shandybina, G. D.; Shakhmin, A. L. Chemical Analysis of Products Obtained by Nanosecond Laser Ablation. *Tech. Phys.* **2000**, *45* (9), 1219–1222. https://doi.org/10.1134/1.1318114.

(7)   Lee, D. W.; Kingery, W. D. Radiation Energy Transfer and Thermal Conductivity of Ceramic Oxides. *J. Am. Ceram. Soc.* **1960**, *43* (11), 594–607. https://doi.org/10.1111/j.1151-2916.1960.tb13623.x.

(8)   Munro, R. G. Evaluated Material Properties for a Sintered α-Al2O3. *J. Am. Ceram. Soc.* **1997**, *28* (8), 1919–1928.

(9)   Nishijima, T.; Kawada, T.; Ishihata, A. Thermal Conductivity of Sintered UO, and Al2O3 at High Temperatures. *J. Am. Ceram. Soc.* **1965**, *48* (1), 31–34. https://doi.org/10.1111/j.1151-2916.1965.tb11788.x.

(10)   Klemens, P. G.; Gell, M. Thermal Conductivity of Thermal Barrier Coatings. *Mater. Sci. Eng. A* **1998**, *245* (2), 143–149. https://doi.org/10.1016/S0921-5093(97)00846-0.

(11)   Braginsky, L.; Shklover, V.; Hofmann, H.; Bowen, P. High-Temperature Thermal Conductivity of Porous Al2O3 Nanostructures. *Phys. Rev. B - Condens. Matter Mater. Phys.* **2004**, *70* (13), 1–7. https://doi.org/10.1103/PhysRevB.70.134201.

(12) Zupančič, M.; Može, M.; Gregorčič, P.; Golobič, I. Nanosecond Laser Texturing of Uniformly and Non-Uniformly Wettable Micro Structured Metal Surfaces for Enhanced Boiling Heat Transfer. *Appl. Surf. Sci.* **2017**, *399*, 480–490. https://doi.org/10.1016/j.apsusc.2016.12.120.

(13) Može, M.; Zupančič, M.; Hočevar, M.; Golobič, I.; Gregorčič, P. Surface Chemistry and Morphology Transition Induced by Critical Heat Flux Incipience on Laser-Textured Copper Surfaces. *Appl. Surf. Sci.* **2019**, *490*, 220–230. https://doi.org/10.1016/j.apsusc.2019.06.068.

(14) Gregorčič, P.; Zupančič, M.; Golobič, I. Scalable Surface Microstructuring by a Fiber Laser for Controlled Nucleate Boiling Performance of High- and Low-Surface-Tension Fluids. *Sci. Rep.* **2018**, *8* (1). https://doi.org/10.1038/s41598-018-25843-5.

(15) Zakšek, P.; Zupančič, M.; Gregorčič, P.; Golobič, I. Investigation of Nucleate Pool Boiling of Saturated Pure Liquids and Ethanol-Water Mixtures on Smooth and Laser-Textured Surfaces. *Nanoscale Microscale Thermophys. Eng.* **2020**, *24* (1), 29–42. https://doi.org/10.1080/15567265.2019.1689590.

(16) Voglar, J.; Gregorčič, P.; Zupančič, M.; Golobič, I. Boiling Performance on Surfaces with Capillary-Length-Spaced One- and Two-Dimensional Laser-Textured Patterns. *Int. J. Heat Mass Transf.* **2018**, *127*, 1188–1196. https://doi.org/10.1016/j.ijheatmasstransfer.2018.07.056.

(17) Bankoff, S. G. Entrapment of Gas in the Spreading of a Liquid over a Rough Surface. *AIChE J.* **1958**, *4* (1), 24–26. https://doi.org/10.1002/aic.690040105.

(18) Jakob, M.; Fritz, W. Versuche Über Den Verdampfungsvorgang. *Forsch. auf dem Gebiete des Ingenieurwesens* **1931**, *2* (12), 435–447. https://doi.org/10.1007/BF02578808.

(19) Sterman, L. S.; Vilemas, Y. The Influence of the State of Heating Surface on Heat Transfer at Boiling. *Int. J. Heat Mass Transf.* **1968**, *11* (2), 347–351. https://doi.org/10.1016/0017-9310(68)90162-2.

(20) Marcus, B. D.; Dropkin, D. Measured Temperature Profiles within the Superheated Boundary Layer above a Horizontal Surface in Saturated Nucleate Pool Boiling of Water. *J. Heat Transfer* **1965**, *87* (3), 333–340. https://doi.org/10.1115/1.3689109.

(21) Allred, T. P.; Weibel, J. A.; Garimella, S. V. Enabling Highly Effective Boiling from Superhydrophobic Surfaces. *Phys. Rev. Lett.* **2018**, *120* (17). https://doi.org/10.1103/PhysRevLett.120.174501.

(22) Može, M.; Zupančič, M.; Golobič, I. Investigation of the Scatter in Reported Pool Boiling CHF Measurements Including Analysis of Heat Flux and Measurement Uncertainty Evaluation Methodology. *Appl. Therm. Eng.* **2020**, *169* (January), 114938. https://doi.org/10.1016/j.applthermaleng.2020.114938.